

Doctoral Dissertation (Abridged)

博士論文（要約）

# Research for Thermoelectric Properties of

## $\text{Sr}_2\text{Si}$ and $\text{Ca}_2\text{Si}$

### ( $\text{Sr}_2\text{Si}$ と $\text{Ca}_2\text{Si}$ の熱電特性に関する研究)

University of Tokyo Graduate School of Frontier Sciences Department of Advanced Materials

Science

新領域創成科学研究科物質系専攻

47-167011

Farhan Mudasar

ファーハン ムダサル

# Acknowledgements

Science can be defined as the organized knowledge of knowing, developing and using something. It can be divided into two types: first-hand and second-hand. First-hand science already exists in nature having scientific foundations, like water cycle, plants, flowers, sunlight, embryonic stages of baby in mother's womb, elements of the periodic table, development of iron ore in earth, functionality of human body and many other examples. Second-hand science is the by-product of first-hand science. Scientists produce second-hand science, which comprises of either discovery or innovation. Human development, processes of eco-system, composition of matter and knowing the capability of human eye exemplifies discovery. Innovation utilizes already discovered scientific knowledge to develop new products and processes. Genetic engineering, renewable energy, synthetic materials and invention of camera based on principles of human eye projects innovation. The best creation of universe is the human being, because they lead the world and uses science for betterment of the world. I would like to thank the Almighty Allah (God), who created universe and gave wisdom to man explicitly to make discoveries and implicitly to make innovations. HE helped me to gain knowledge throughout my life and to achieve the milestone of completing my doctoral studies.

I would like to thank Japanese government, who gave me MEXT scholarship for PhD studies in Japan. I would like to express my sincere gratitude to my supervisor, Prof. Kaoru Kimura, for accepting me as a PhD student in his laboratory. He trained me professionally like a mentor and affectionately like a father. He was always patient, very kind, and supportive. Although my background was from material science only, but my research included concepts from physics and material science both. Dr. Kimura endeavoured his best to make me understand concepts of

physics to finish PhD in three years. I believe he spent more time with me than I deserved during the tenure of my doctoral studies. His critical analysis of the results rationally and disagreement upon the doubtful ones, shows his command over his research area. In my opinion, he can be rightly said as one of the best professor in the world, having knowledge of his research area and professional skills to train students. I feel fortunate enough, that I had an opportunity to work in his group and always enjoyed his knowledgeable discussions.

I would like to appreciate the support extended to me by my lab members, Dr. Yukari Katsura and Dr. Koicho Kitahara, who always attended my bi-weekly meetings with my supervisor. Without their input it was impossible for me to finish my research efficiently. I would like to thank to Dr. Katsura, her calculations work became the startle of this research. I appreciate her technical knowledge and contributions in this research. I owe special thanks to Dr. Kitahara for his continuous help in experimental work and deliberating results. He has extensive knowledge of materials science, physics, and experimental work, which proved to be very helpful in conducting my experiments and understanding results. He helped me three consecutive years, having many sleepless nights of experiments in laboratory, and interestingly I have never seen him frustrated or tired of teaching. He is dedicated to his profession and was super kind to me.

I would also like to thank my lab members Mr. Tobita Kazuki and Mr. Yutaka Iwasaki, with whom I often discussed my research in a friendly manner. Mr. Iwasaki had command on physical concepts and he helped me conceptualizing the ideas. Mr. Kazuki was a generous person, at many occasions he did hours long discussions related to my research. He remained passionate in solving research problems. This proved that he is a noble person, who is kind, patient, dedicated to his profession. He also helped me in areas other than research.

I owe special thanks to Ms. Makiko Nakano for helping in official works at campus and her guidance in understanding Japanese culture and traditions.

I would also like to thank my other laboratory members who made my stay convenient, especially Mr. Takahiro Ishigami (tutor), Mr. Hideyasu Ouchi (tutor), Dr. Takanobu Hiroto, Dr. Naoki Sato, Mr. Hitoshi Yamamura, Mr. Jang Jeonghwan, Miss. Sahar Ayachi, and Mr. Shohei Yamasaki.

I owe special thanks to my late parents (Mudasar Tanzim Qureshi and Naheeda Mudasar), it was not possible without their efforts. I would also like to thank my brothers, Mr. Omair Mudasar, Mr. Sanan Mudasar, Mr. Roshaan Mudasar, and Mr. Fahad Mudasar, without their continuous love, efforts, support and appreciation it could not happen. I would like to thank my loving aunts, Ms. Saeeda Akhtar, Ms. Waheeda Bano, Ms. Jaheeda Akhtar, who looked after me and my brothers after our mother passed away, their efforts could never be forgotten. I am also grateful to my relatives, uncles, cousins, who always prayed for my success. I would also like to thank friends, Dr. Babar Javed and others, outside my university who always encouraged and supported me in difficult situations. I would also like to thank people who helped me in reaching this stage and whom I forgot to mention here.

“Thank you very much all of you. I pray to God Almighty to give you best reward in this world and hereafter”.

Finally, I would again thank to Almighty Allah (God) who gave me opportunities (first-hand science, MEXT scholarship, Prof. Koaru Kimura and laboratory members, family members, relatives, friends) to reach this point, without His blessings it was impossible.

# Dedication

“To my late parents, brothers, relatives, friends and everyone who contribute to make this world a better place”.

## **Quran**

“Indeed, this Qur'an guides to that which is most suitable and gives good tidings to the believers who do righteous deeds that they will have a great reward.” (Al-Israa, 17:9)

“Worship Allah and associate nothing with Him, and to parents do good, and to relatives, orphans, the needy, the near neighbor, the neighbor farther away, the companion at your side, the traveler, and those whom your right hands possess. Indeed, Allah does not like those who are self-deluding and boastful.” (An-Nisa, 4:36)

“(God is) the one who created the night, the day, the sun and the moon. Each one is traveling in an orbit with its own motion.” (Al-Anbya, 21:33)

## **Statements of Prophet Muhammad PBUH**

“Seeking knowledge is compulsory on every Muslim.”

“Wisdom is the lost property of the believer.”

“Whoever follows a path seeking knowledge, Allah will make his path to paradise easy.”

# Contents

Summary.....	1
Acknowledgements.....	5
Dedication.....	8
List of Figures.....	13
List of Tables.....	18
1. Introduction.....	19
1.1 Why Thermoelectrics ?.....	19
1.2 TE concepts.....	22
1.2.1 Peltier Effect/Thermoelectric heating/cooling.....	22
1.2.2 Seebeck Effect/Thermoelectric power generation.....	22
1.2.3 Thermoelectric figure of merit.....	24
1.2.4 Power conversion efficiency.....	25
1.2.5 Carrier concentration.....	26
1.2.6 Seebeck coefficient.....	27
1.2.7 Electrical conductivity.....	28
1.2.8 Thermal conductivity.....	30
1.2.8.1 Slack's model of thermal conductivity.....	30
1.3 Classification of TE materials.....	31
1.3.1 Silicide TE materials.....	31
1.3.1.1 Metal silicides.....	32
1.3.1.2 Alkaline earth silicides.....	34
1.3.1.2.1 Magnesium silicide ( $\text{Mg}_2\text{Si}$ ) alloys.....	34

1.3.1.2.2	Calcium silicide ( $\text{CaSi}$ , $\text{Ca}_2\text{Si}$ , and $\text{Ca}_5\text{Si}_3$ ) .....	36
1.4	Effect of Humidity and Oxide on TE properties of $\text{Mg}_2\text{Si}$ .....	39
1.5	Composite Effect .....	42
1.5.1	Nanostructures, and Nanostructure bulk materials .....	42
1.5.2	Mechanisms for improving TE materials by introduction of nanoparticles .....	44
1.5.2.1	Alloying.....	44
1.5.2.2	Energy filtering.....	45
1.6	Improving $ZT$ by micron size metallic phase .....	46
1.7	Simultaneous decrease in electrical resistivity and increase in Seebeck coefficient.....	48
2.	The purpose of this research.....	51
2.1	Why $\text{Sr}_2\text{Si}$ and $\text{Ca}_2\text{Si}$ ?.....	51
3.	Strontium silicides ( $\text{Sr}_2\text{Si}$ , $\text{Sr}_5\text{Si}_3$ , and their composites) .....	56
3.1	Experimental .....	56
3.2	Results.....	58
3.2.1	Phase analysis .....	58
3.2.1.1	After synthesis.....	58
3.2.1.2	After SPS .....	60
3.2.1.3	After ZEM measurements .....	62
3.2.2	Microstructure analysis .....	65
3.2.3	Thermoelectric properties .....	68
3.3	Discussion .....	73
3.3.1	Effect of composite on thermoelectric properties .....	73
3.3.2	Origin of low lattice thermal conductivity .....	77
3.3.3	Lowest thermal conductivity silicide.....	81

3.4	Summary .....	82
4.	Calcium silicides ( $\text{Ca}_2\text{Si}$ , $\text{Ca}_5\text{Si}_3$ , and their composites) .....	84
4.1	Experimental .....	84
4.2	Results .....	85
4.2.1	Phase analysis .....	85
4.2.1.1	After synthesis .....	85
4.2.1.2	After SPS .....	86
4.2.1.3	After ZEM measurements .....	89
4.2.2	Microstructure analysis .....	92
4.2.3	Thermoelectric properties .....	99
4.3	Discussion .....	104
4.3.1	Effect of composite on thermoelectric properties .....	104
4.3.2	Origin of low lattice thermal conductivity .....	108
4.3.3	Lowest thermal conductivity silicide .....	110
4.4	Summary .....	111
5.	Comparison of $\text{Sr}_2\text{Si}$ , $\text{Ca}_2\text{Si}$ with high $ZT$ $\text{Mg}_2\text{Si}$ .....	113
5.1	Oxide impurity and crystallinity .....	113
5.2	Microstructure .....	117
5.3	TE properties .....	118
5.4	Discussion .....	120
5.5	Summary .....	125
6.	Conclusions and Perspective .....	126
6.1	Conclusions .....	126
6.2	Perspectives .....	127



Publications .....	129
Conferences .....	129
References .....	130

# List of Figures

Figure 1-1 Global production of fossil energy from 1800 to 2010 [4] .....	19
Figure 1-2 Estimated world energy use of 2012 in PJ – excluding fuel processing and non-energy use (total consumption of primary energy carriers: 474.171 PJ). [5] .....	20
Figure 1-3 CO <sub>2</sub> emission trends from 1971 to 2009 by fuel [2] .....	21
Figure 1-4 TE heat engines. (A) When current is run across a TE junction, it heats or cools through the Peltier effect, depending on the direction of the current flow. (B) When heat flows across the junction, electrical current is generated through the Seebeck effect. (C) Practical TE generators connect large numbers of junctions in series to increase operating voltage and spread heat flow. [6] .....	23
Figure 1-5 Plot shows some of best $ZT$ materials [7] .....	24
Figure 1-6 Plot shows the thermoelectric conversion efficiency as a function of differential operating temperature and $ZT$ [9]. .....	25
Figure 1-7 Plot shows the effect of carrier concentration on the $ZT$ values of $Mg_xPb_{1-x}Te$ : Na, $PbTe_{1-x}Se_x$ , $Pb_{1-x}Mn_xTe$ : Na, and $La_{3-x}Te_4$ at different temperatures [8] .....	26
Figure 1-8 Plot shows the variations in the electrical properties of a thermoelectric material as a function of carrier concentration [11]. .....	27
Figure 1-9 Schematic shows the room-temperature electrical conductivity of various materials [12] .....	29
Figure 1-10 Influence of temperature on electrical conductivity of materials synthesized by various methods [8] .....	29
Figure 1-11 Cost of various thermoelectric materials based on the raw material costs of the constituent elements [18] .....	32
Figure 1-12 Temperature dependence of TE properties with Bi doping concentration [22] .....	35
Figure 1-13 Temperature dependence of TE properties of $CaSi$ and $Ca_5Si_3$ (a) electrical conductivity, (b) seebeck coefficient, (c) thermal conductivity, and (d) $ZT$ [23] .....	37
Figure 1-14 Powder XRD diffraction patterns of the Sb-doped $Mg_2Si$ TE-legs fabricated by SPS using raw material powders exposed to atmosphere with the humidity of 30, 60, and 80% for 24 hours [25] .....	39

Figure 1-15 Thermograms of TG (a) and DTA; (b) analysis of $\text{Mg}_2\text{Si}$ samples containing 0 wt.%, and 4 wt.% $\text{MgO}$ [25].....	40
Figure 1-16 (a) Crystallite size trend after each synthesis process and after functional analyses, and (b) $\text{MgO}$ amount in the commercial material and after the different thermal processes [26]......	41
Figure 1-17 Schematic illustration of general strategies for improving thermoelectric performance of materials by modifying the structures from macro- to nanoscale. a–d Change in dimensionality and size: a bulk, b superlattice, c thin-film, d nanowires; e–h Modification of the grain structures in bulk: e micrometer grains, f nanometer grains, g mixture of grains with different sizes, h mixture of nanoparticles with different compositions; i–j Composites of embedded nanoparticles in a bulk matrix, formed by: i co-compaction of a physical mixture of the two components, j in situ formation of nanosize precipitates within the bulk matrix [27]. .....	43
Figure 1-18 (a) All-scale hierarchical architectures exhibiting the scattering of phonons of different mean free paths and (b) cumulative distribution function of lattice thermal conductivity with respect to the phonon mean free path in Si or PbTe bulk [15]. .....	44
Figure 1-19 Schematic of the semiconductor host with metallic nanoinclusions. Panel (b) shows an example of the calculated potential $V(r)$ and the energy diagram for PbTe at $T = 300 \text{ K}$ , $n = 2.5 \times 10^{19} \text{ cm}^{-3}$ , $V_B = -0.11 \text{ eV}$ , and $R = 1.5 \text{ nm}$ . Panel (c) illustrates the concept of energy filtering: low energy electrons scatter strongly with the potential, but high energy electrons are unaffected. The calculated electronic relaxation time for the potential of panel (b) is also shown [37]. .....	46
Figure 1-20 SEM micrographs of $\text{Sr}_{0.8}\text{La}_{0.06}\text{Ti}_{0.8}\text{Nb}_{0.2}\text{O}_3$ samples: (a) control, (b) prepared with Fe additions, (c) prepared with Cu additions [38]. .....	47
Figure 1-21 Thermoelectric properties of the $\text{Sr}_{0.8}\text{La}_{0.06}\text{Ti}_{0.8}\text{Nb}_{0.2}\text{O}_3$ (control) and the Cu-containing and Fe-containing samples as a function of temperature: (a) electrical resistivity, (b) Seebeck coefficient, (c) thermal conductivity, (d) figure of merit, $ZT$ . Data for doped single crystal $\text{SrTiO}_3$ is from literature for comparison [38]. .....	48
Figure 1-22 Temperature dependence of (a) Seebeck coefficient and (b) electrical resistivity of $\text{Ca}_{3-x}\text{Bi}_x\text{Co}_4\text{O}_9$ with $x = 0$ to $0.15$ [39]. .....	49
Figure 1-23 (a) Electrical resistivity and (b) Seebeck coefficient of non-doped $\text{YB}_{22}\text{C}_2\text{N}$ (●) and $\text{VB}_2$ doped/seeded $\text{YB}_{22}\text{C}_2\text{N}$ [41]. Heat treatment changed $\text{VB}_2$ content 11 vol% (□) to 9 vol% (■) for same sample. Data for a heavily 16 vol% doped/seeded sample with multiple heating (x) is also shown. (c) EDS mapping of V of $\text{VB}_2$ doped/seeded $\text{YB}_{22}\text{CN}$ , the heavily 16 vol% doped/seeded sample with multiple heating [40]. .....	50
Figure 2-1 The calculated band structure (left) and the total density of states (right) of (a) $\text{Mg}_2\text{Si}$ , (b) $\text{Ca}_2\text{Si}$ , and (c) $\text{Sr}_2\text{Si}$ [42] .....	53

Figure 2-2 Carrier concentration dependence of $A$ of $Mg_2Si$ and $Ca_2Si$ , calculated in intervals of 100 K. Solid and broken lines correspond to hole-doped and electron-doped cases [43].	54
Figure 3-1 XRD patterns of all samples after synthesis.	59
Figure 3-2 XRD patterns of all samples after SPS	61
Figure 3-3 XRD patterns of all samples after ZEM measurements.	64
Figure 3-4 Ratios of XRD peak intensities of secondary phases ( $Sr_3SiO$ , $Sr_5Si_3$ ) and main phase ( $Sr_2Si$ ). $R_{311/21}$ is the ratio of the $Sr_3SiO$ (0 2 2) peak to $Sr_2Si$ (0 2 0) peak. $R_{53/21}$ is the ratio of the $Sr_5Si_3$ (2 0 -4) peak to $Sr_2Si$ (0 2 0) peak.	65
Figure 3-5 (a) BEI, and (b)–(d) Elemental mapping of composite sample D by SEM-EDS.	66
Figure 3-6 Magnified SEM micrographs of composite sample D. (a) BEI, and (b) SEI.	67
Figure 3-7 Temperature dependence of (a) electrical resistivity $\rho$ , (b) Seebeck coefficient $S$ , and (c) power factor $P$	69
Figure 3-8 Temperature dependence of (a) total thermal conductivity $\kappa$ , (b) electronic thermal conductivity $\kappa_{el}$ , and (c) lattice thermal conductivity $\kappa_{lat}$ .	71
Figure 3-9 Temperature dependence of dimensionless figure of merit $ZT$	72
Figure 3-10 (a)–(e) Dependence of transport properties at 373 K on $R_{311/21}$ , i.e., the amount of $Sr_3SiO$ phase present in the system.	75
Figure 3-11 (a)–(e) Dependence of transport properties at 373 K on $R_{53/21}$ , i.e., the amount of $Sr_5Si_3$ phase present in the system.	76
Figure 3-12 Arrhenius plot of electrical resistivity versus inverse temperature. Error in TE properties was calculated by considering uncertainty in sample dimensions and instruments	77
Figure 3-13 Relationship between $(M\delta(\theta_D)^3 / N^{2/3}T, T=300\text{ K})$ and $\kappa_{lat}$ for samples B ( $Sr_2Si$ ) and H ( $Sr_5Si_3$ ), together with literature data for $BaSi_2$ , $SrSi_2$ , $LaSi$ , and $Mg_2Si$ taken from Ref. [13].	81
Figure 4-1 XRD patterns of all samples after synthesis.	86
Figure 4-2 XRD patterns of all samples after SPS	88
Figure 4-3 XRD patterns of all samples after ZEM measurements.	91

Figure 4-4 Ratios of XRD peak intensities of secondary phases ( $\text{Ca}_3\text{SiO}$ , $\text{Ca}_5\text{Si}_3$ ) and main phase ( $\text{Ca}_2\text{Si}$ ). $R_{311/21}$ is the ratio of the $\text{Ca}_3\text{SiO}$ (0 2 2) peak to $\text{Ca}_2\text{Si}$ (2 1 1) peak. $R_{53/21}$ is the ratio of the $\text{Sr}_5\text{Si}_3$ (2 0 4) peak to $\text{Sr}_2\text{Si}$ (2 1 1) peak. ....	92
Figure 4-5 (a) BEI, (b) SEI, and (c)–(e) Elemental mapping of composite sample Y by SEM-EDS. ....	94
Figure 4-6 (a) BEI, and (b) SEI of composite sample Y by SEM-EDS at low magnification.....	95
Figure 4-7 BEI of composite sample Y at high magnification: (a) EDS point analysis, and (b) phases labelling .....	97
Figure 4-8 Temperature dependence of (a) electrical resistivity, (b) log of electrical resistivity, (c) Seebeck coefficient, (d) power factor, and (e) log of power factor, of non-composite and composite samples with literature data (unfilled markers, dashed line) of $\text{Ca}_5\text{Si}_3$ .....	100
Figure 4-9 Temperature dependence of (a) total thermal conductivity $\kappa$ , (b) electronic thermal conductivity $\kappa_{\text{el}}$ , and (c) lattice thermal conductivity $\kappa_{\text{lat}}$ , with $\text{Ca}_5\text{Si}_3$ from literature (unfilled markers, dashed line) .....	102
Figure 4-10 Temperature dependence of dimensionless figure of merit $ZT$ , with $\text{Ca}_5\text{Si}_3$ data from literature.....	103
Figure 4-11 (a)–(e) Dependence of transport properties at 373 K on $R_{311/21}$ , i.e., the amount of $\text{Ca}_3\text{SiO}$ phases present in the system, respectively. ....	106
Figure 4-12 (a)–(e) Dependence of transport properties at 373 K on $R_{53/21}$ , i.e., the amount of $\text{Ca}_5\text{Si}_3$ phases present in the system, respectively. ....	107
Figure 4-13 Relationship between $(M\delta(\theta_D)^3 / N^{2/3}T, T=300 \text{ K})$ and $\kappa_{\text{lat}}$ for samples W ( $\text{Ca}_2\text{Si}$ ), together with the literature data for $\text{BaSi}_2$ , $\text{SrSi}_2$ , $\text{LaSi}$ , and $\text{Mg}_2\text{Si}$ from [13] and $\text{Ca}_5\text{Si}_3$ from [23]. ....	110
Figure 5-1 (a) XRD data of non-composite (B) and maximum $ZT$ composite (G) samples of $\text{Sr}_2\text{Si}$ , (b) XRD data of non-composite (W) and maximum $ZT$ composite (Z) samples of $\text{Ca}_2\text{Si}$ , (c) XRD patterns for $\text{Mg}_2\text{Si}_{1-x}\text{Bi}_x$ samples, (a, c, e) after consolidation by SPS method, (b, d, f) after annealing, Nieroda et. al. [60], (d) Refined X-ray powder profile of $\text{Mg}_2\text{Si}_{1-x}\text{Bi}_x$ . Red line represents the experimental data and the black line represents the calculated powder profile, M. Ioannou et. al. [62], and (e) XRD data from $\text{Mg}_2\text{Si}$ powder and from samples 1 and 3 after compaction (SPS) and measurement. The powder shows $\text{Mg}_2\text{Si}$ and minimal traces of Si, while the compacted samples show visible peaks corresponding to MgO and Si as secondary phases [52]. ....	116

Figure 5-2 Backscattered electron image and elemental mapping of (a)-(d) composite sample D of  $\text{Sr}_2\text{Si}$ , (e)-(h) composite sample Z of  $\text{Ca}_2\text{Si}$ , and (i)-(l) Sb doped  $\text{Mg}_2\text{Si}$ ,  $\text{Mg}_2\text{Si}_{0.9875}\text{Sb}_{0.0125}$ , D. Boor et. al. [52] ..... 117

Figure 5-3 Temperature dependence of (a) electrical resistivity, (b) log of electrical resistivity, (c) Seebeck coefficient, (d) power factor, and (e) log of power factor, of non-composites and composites (max.  $ZT$  samples) of  $\text{Sr}_2\text{Si}$  and  $\text{Ca}_2\text{Si}$ , with literature data (unfilled markers, dashed line) of undoped and doped  $\text{Mg}_2\text{Si}$  ..... 119

Figure 5-4 Temperature dependence of (a) total thermal conductivity  $\kappa$ , (b) lattice thermal conductivity  $\kappa_{\text{lat}}$ , and (c)  $ZT$ , of non-composites and composites (max.  $ZT$  samples) of  $\text{Sr}_2\text{Si}$  and  $\text{Ca}_2\text{Si}$ , with literature data (unfilled markers, dashed line) of undoped and doped  $\text{Mg}_2\text{Si}$ ..... 120

Figure 5-5 Temperature dependence of literature [52]  $\text{Mg}_2\text{Si}$  with varying amounts (wt. %) of  $\text{MgO}$ , (a)-(d) TE properties and (e) hall mobility,  $\mu_{\text{H}}$ . Seebeck coefficient and thermal conductivity of all samples are comparable, the electrical conductivity differs significantly among the samples and shows a clear correlation with  $\text{MgO}$  content. .... 124

# List of Tables

Table 1-1 Some parameters of silicide materials, which could be used in thermoelectric devices [17].	34
Table 1-2 List of main properties of silicides [16]	38
Table 3-1 Sample details for all samples, where the SPS time is the time at maximum temperature, where h is hour.	57
Table 3-2 Phases and relative densities after SPS, relative density is with respect to $\text{Sr}_2\text{Si}$ phase.	58
Table 3-3 Elemental composition of phases determined by EDS point analysis.	67
Table 3-4 Thermophysical properties of strontium silicide samples together with the literature data.	79
Table 4-1 Sample details for all samples, where the SPS time is the time at maximum temperature, where h is hour.	84
Table 4-2 Phases and relative densities after SPS, relative density is with respect to $\text{Ca}_2\text{Si}$ phase.	89
Table 4-3 Summary of EDS results of all points of micrograph shown in Figure 4-6	96
Table 4-4 Summary of EDS results of all points of micrograph shown in Figure 4-7	98
Table 4-5 Thermophysical properties of calcium silicide samples together with the literature and strontium silicides (this work) data.	109
Table 5-1 Properties of some selected materials from literature at room temperature and from this research at $\sim 373$ K.	123

# 1. Introduction

## 1.1 Why Thermoelectrics ?

In the beginning of 18<sup>th</sup> century, industrial revolution was started, which mainly dependent on fossil fuel. Since then consumption of fossil fuels have been increasing annually, reaching about  $10^3$  million tons of oil equivalent per year, Figure 1-1. Currently, fossils fuels provides 80% of primary energy to the world, contribution of oil, coal, natural gas are 32.8%, 27.2%, and 20.9%, respectively [2]. Largest energy sources other than fossil fuels are hydroelectric dams, nuclear power, and combustible biomass and waste, contributing 2.3%, 5.8%, and 10.2%, respectively, which is small portion of total energy supply [2]. Geothermal, wind, solar, and other energy sources supply only 0.8 % of the total energy. Precisely, wind power (0.2%) and direct solar energy (0.1%) contributes 23 and 12 Mtoe of energy, respectively [3]. These statistics predicts that fossil fuels will continue to be the main source of energy in future.

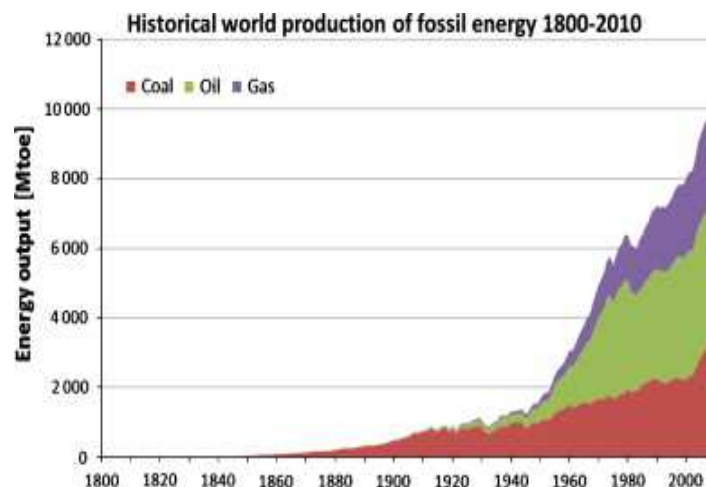
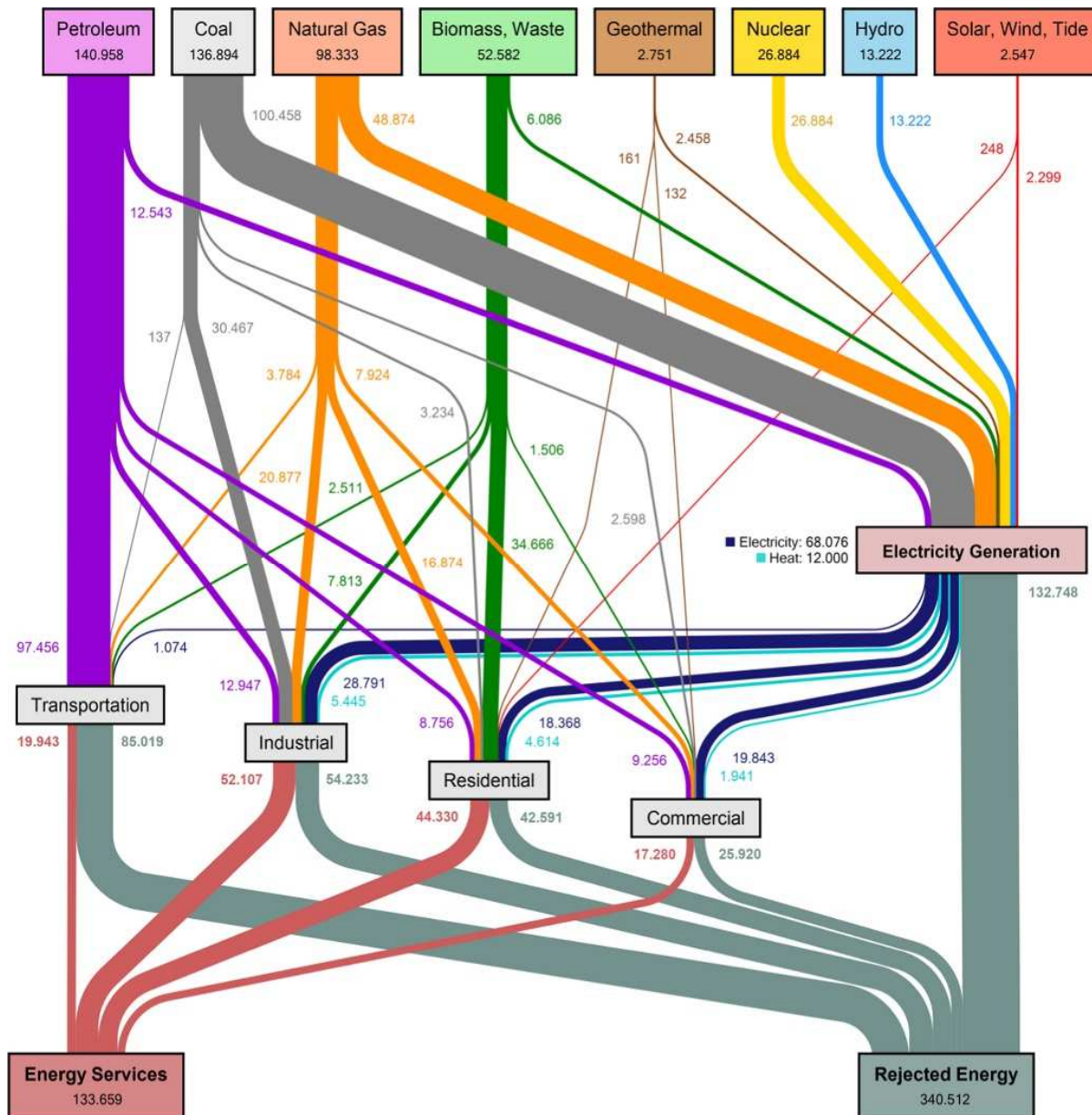


Figure 1-1 Global production of fossil energy from 1800 to 2010 [4]



As shown in Figure 1-2, about 72% (340.512 PJ) of energy used in services is wasted during conversion. Waste heat existed in all energy conversion steps and is rejected in form of heat in to the environment. Waste heat can be used either by the same process which evolve heat or it can be used for some other useful purpose, in former case process efficiency can be increased [5].



**Figure 1-2 Estimated world energy use of 2012 in PJ – excluding fuel processing and non-energy use (total consumption of primary energy carriers: 474.171 PJ). [5]**

Moreover, energy production has connected issue of emissions, CO<sub>2</sub> and other greenhouse gases. About 70 percent of greenhouse gases comes out from energy used by human beings, with largest input from fossil fuels, Figure 1-3. Nearly 30 billion tons of CO<sub>2</sub> was discharged in 2008, which was double of 1970. Global warming, climate change and greenhouse gasses produced by fossil fuels are strongly related.

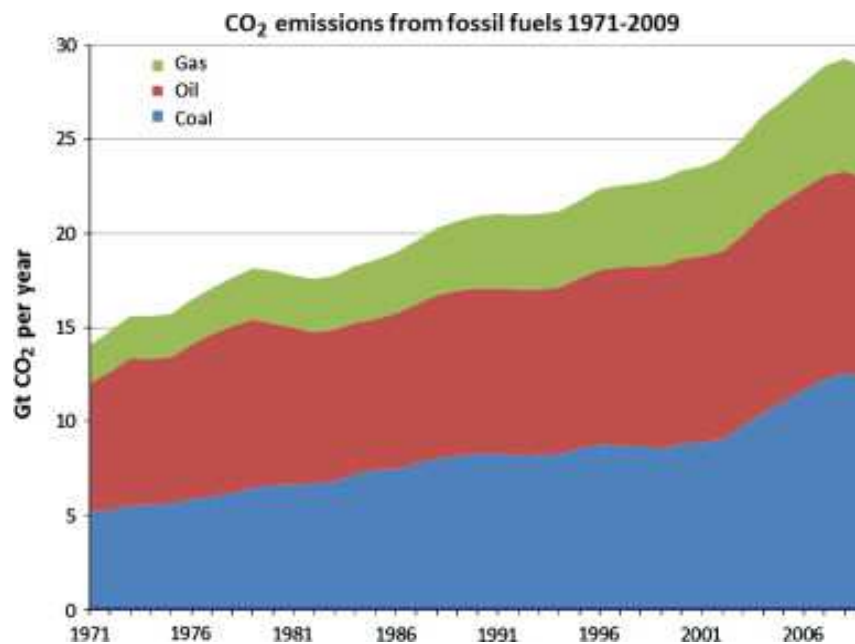


**Figure 1-3 CO<sub>2</sub> emission trends from 1971 to 2009 by fuel [2]**

It is the need of the time to focus attention on technologies which can decrease greenhouse emissions and fossil fuel usage. Thermoelectric devices are solid state semiconductor devices that convert electricity into thermal energy for heating or cooling, or waste heat into electricity. In later case, it can produce cleaner form energies by decreasing CO<sub>2</sub> emissions and greenhouse gas emissions.

## **1.2 TE concepts**

TE devices are solid-state heat engines. In normal air conditioners, two phase fluid is used like R-22, whereas in TE generators electrons/holes are used as working fluid. Figure 1-4 shows working of TE device [6].

### **1.2.1 Peltier Effect/Thermoelectric heating/cooling**

Peltier in 1834 found that if a current is applied across the junction of two different conductors then either heating or cooling occurred across the junctions, reversing current will reverse heating/cooling. Figure 1-4 (A) demonstrates this phenomenon, illustrating why this happens. In n-type, electric current generate by electrons and in p-type by holes in reverse direction. When voltage is applied across the p- and n-type junction then electron and hole pair are produced near junction. Electron and holes takes energy from junction area and move away in n- and p-type materials, respectively, causing cooling. This electron and hole pair recombines and releases energy on the other end, causing heating. [6]

### **1.2.2 Seebeck Effect/Thermoelectric power generation**

Seebeck in 1821 found deflection in needle of a magnet when junctions of two different conductors were exposed to temperature difference. Current flows in series and heat flows in parallel. This phenomenon is foundation of TE power generation. In Figure 1-4 (B), if top of junction is heated and opposite is cooled by keeping a temperature difference then electron and hole pairs will generate. This electron and hole pair will absorb energy from hot side, then recombine and release energy on cold side. As a result, potential difference/seebeck voltage generates, net voltage appears across the ends of the thermoelectric elements/legs. Electrical power is taken by making

connection of TE elements with external load. In Figure 1-4 (C) thermoelectric module is shown, constructed in such a way that all junctions on one side heat and those on the other side cool [6].

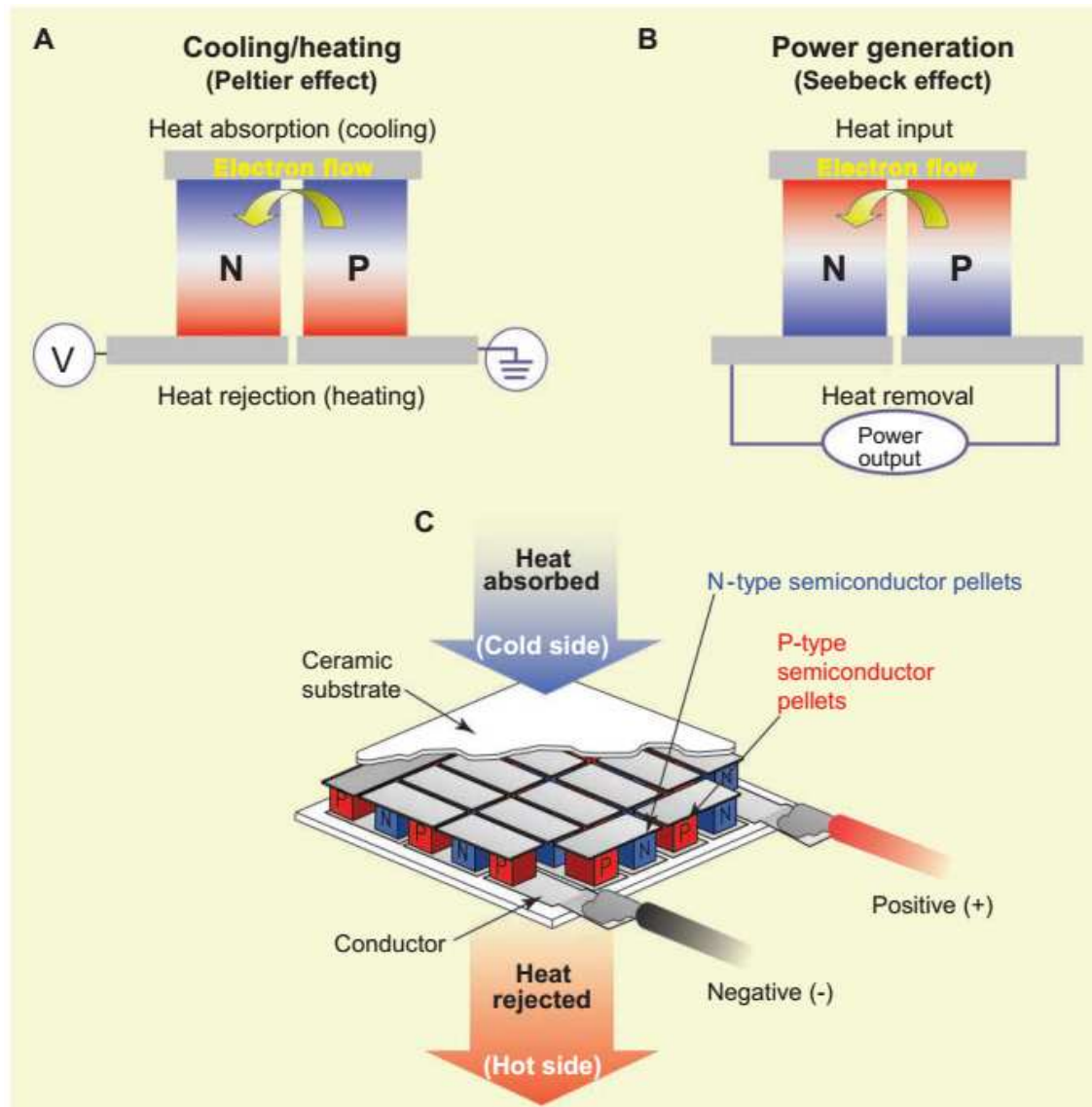


**Figure 1-4 TE heat engines. (A) When current is run across a TE junction, it heats or cools through the Peltier effect, depending on the direction of the current flow. (B) When heat flows across the junction, electrical current is generated through the Seebeck effect. (C) Practical TE generators connect large numbers of junctions in series to increase operating voltage and spread heat flow. [6]**

### 1.2.3 Thermoelectric figure of merit

The efficiency of thermoelectric material is given by dimensionless figure merit ( $ZT$ ), Eq. 1-1, where  $\sigma$  is the electrical conductivity,  $S$  is the Seebeck coefficient, and  $\kappa$  is the thermal conductivity of the material. Best TE materials should have a large  $S$ ,  $\sigma$ , and a low  $\kappa$  to 1) generate a large potential difference across two ends by reducing the Joule heating effect, and 2) to keep a large temperature difference, respectively. Figure 1-5 illustrates the  $ZT$  values of the selected materials with good  $ZT$ .

$$ZT = \frac{S^2 \sigma T}{\kappa} \quad \text{Eq. 1-1}$$

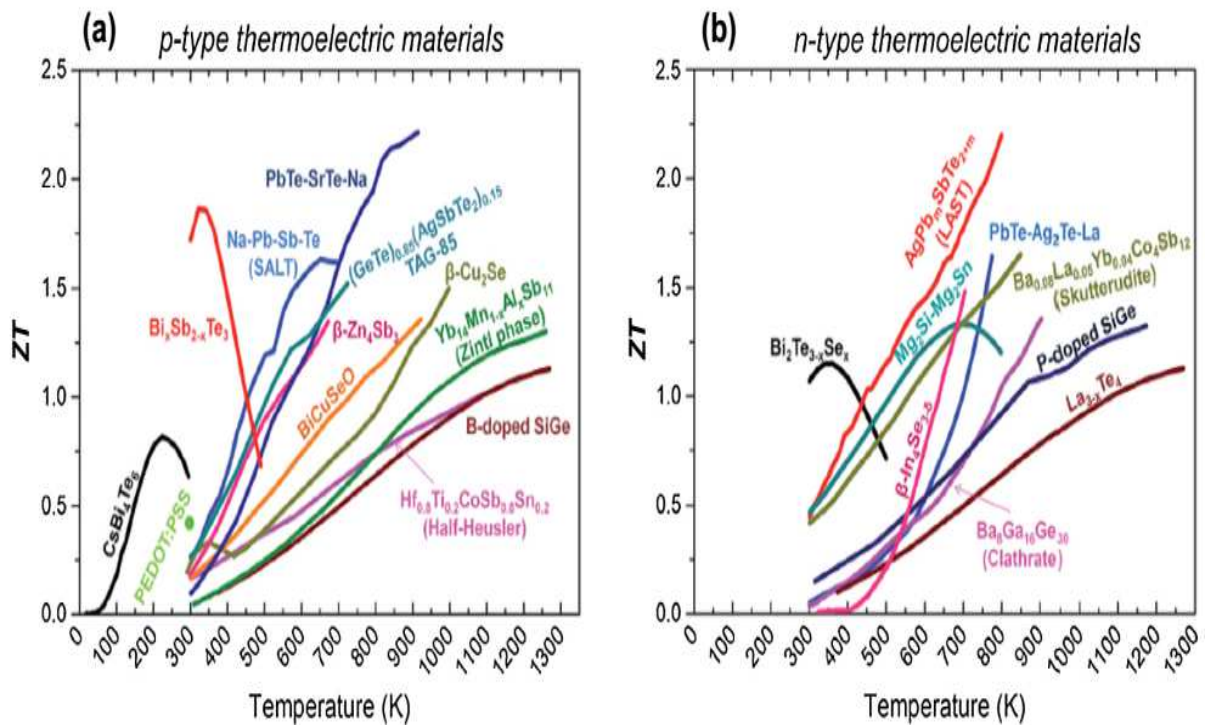


Figure 1-5 Plot shows some of best  $ZT$  materials [7]

### 1.2.4 Power conversion efficiency

The product of  $ZT$  dependent parameter and carnot efficiency gives the TE device efficiency, given in Eq. 1-2, where  $T_{\text{cold}}$  and  $T_{\text{hot}}$  are the cold and hot side temperatures, respectively. The relationship of  $ZT$ , conversion efficiency and hot side temperatures are shown in Figure 1-6. The conversion efficiency is 10-15% for  $ZT$  equal to 1 when  $T_{\text{hot}} = 700\text{-}1025$  K.  $ZT$  greater than 2 is previously attained. For practical applications  $ZT > 1$  is required to attain efficiency of greater than 10% [8].

$$\eta = \frac{\Delta T}{T_{\text{hot}}} \frac{\sqrt{1+ZT}-1}{\sqrt{1+ZT}+\frac{T_{\text{cold}}}{T_{\text{hot}}}} \quad \text{Eq. 1-2}$$

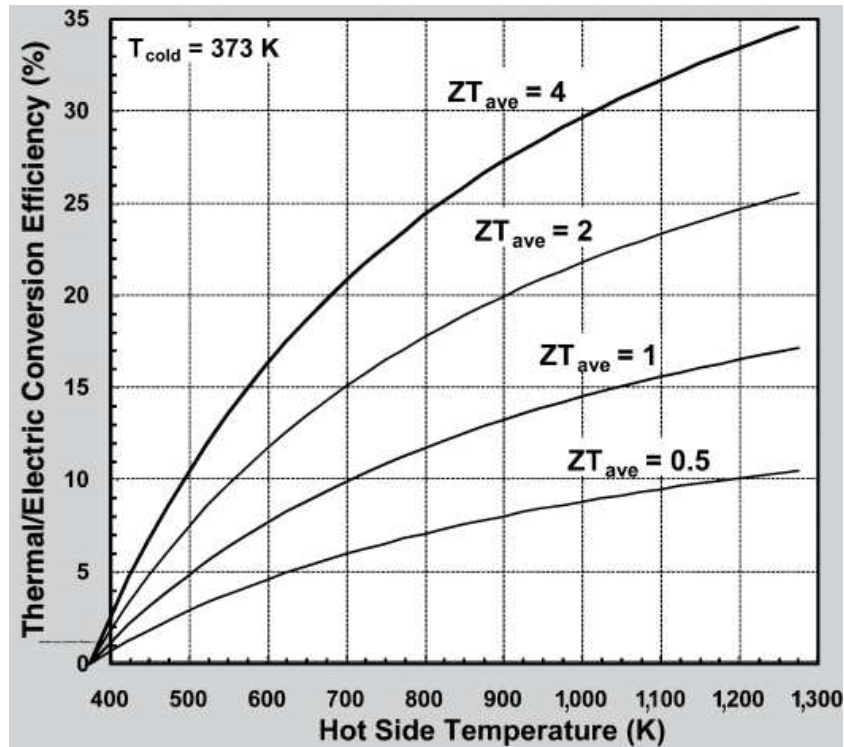


Figure 1-6 Plot shows the thermoelectric conversion efficiency as a function of differential operating temperature and  $ZT$  [9].



## 1.2.5 Carrier concentration

$\sigma$  and  $S$  depend upon carrier concentration. In TE research carrier concentration is optimized to avoid bipolar conduction. Charge carrier type, carrier concentration, and mobility are determined by Hall effect measurements. Nature of dopant and its concentration also effects charge carrier type and concentration. Effect of carrier concentration on  $ZT$  is shown in Figure 1-7, in relationship with temperature and dopant. Carrier concentration also varies with temperature.  $\sigma$  increases at high temperature due to increase in carrier concentration, resulting in high  $ZT$ . Mobility can have significant effects on  $\sigma$ . Other factors effecting mobility are grain boundaries, secondary phases, alloying, doping [8].

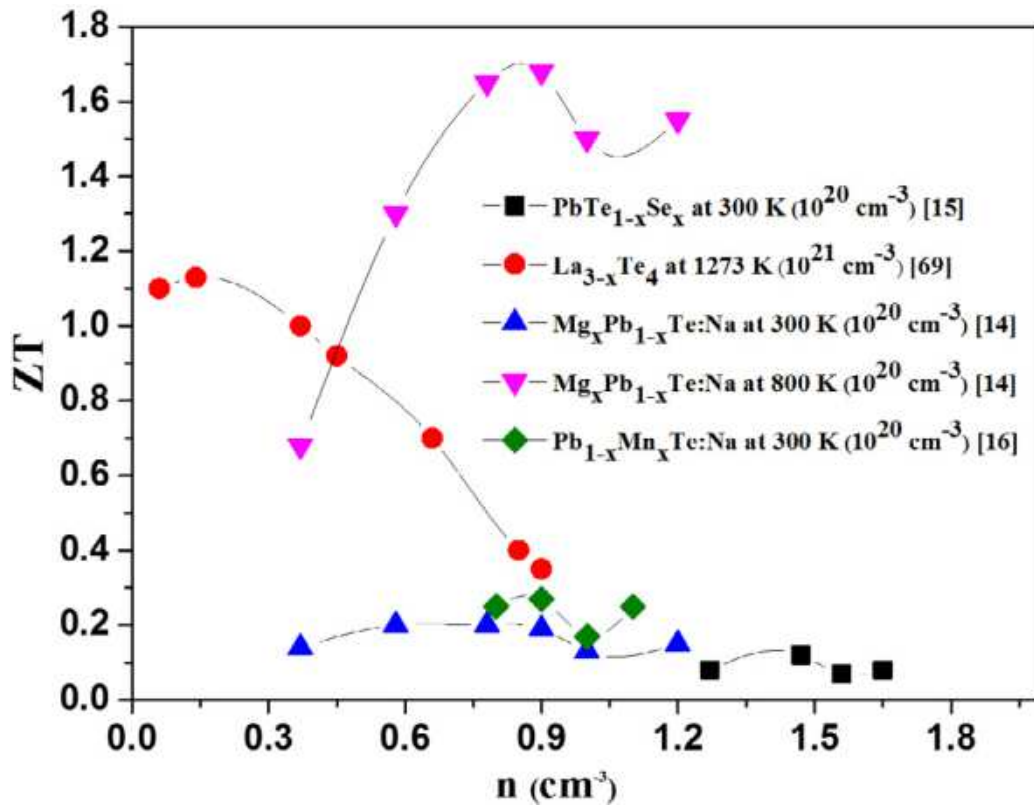


Figure 1-7 Plot shows the effect of carrier concentration on the  $ZT$  values of  $\text{Mg}_x\text{Pb}_{1-x}\text{Te:Na}$ ,  $\text{PbTe}_{1-x}\text{Se}_x$ ,  $\text{Pb}_{1-x}\text{Mn}_x\text{Te:Na}$ , and  $\text{La}_{3-x}\text{Te}_4$  at different temperatures [8]

## 1.2.6 Seebeck coefficient

Mott relation for Seebeck coefficient is given below [10];

$$\alpha = \frac{\pi^2 \kappa_B}{3 q} \kappa_B T \left( \frac{1}{n} \frac{dn(E)}{dE} + \frac{1}{\mu} \frac{d\mu(E)}{dE} \right)_{E=E_F} \quad \text{Eq. 1-3}$$

In Eq. 1-3,  $q$  is the electronic charge,  $n(E)$  is the charge carrier density at energy  $E$ ,  $\mu(E)$  is the mobility at the energy,  $E_F$  is the Fermi energy, and  $T$  is the temperature. Good TE materials should have  $S$  greater than 200  $\mu\text{V/K}$ , which shows high voltage producing capability.  $S$  depends upon bandgap and carrier concentration.  $S$  has non-linear relationship with temperature. More precisely,  $S$  depends upon crystal structure, composition, carrier concentration, and absolute temperature. Figure 1-8 shows the relationship of  $S$ ,  $\sigma$ ,  $\kappa$ , and carrier concentration. At higher carrier concentration,  $\sigma$  increases and  $S$  decreases. Maximum  $ZT$  can be obtained by maximizing power factor,  $P$ , which is obtained by adjusting carrier concentration, where  $P$  is product of  $S^2$  and  $\sigma$ . Degenerate semiconductor can be best choice in this regard [8].

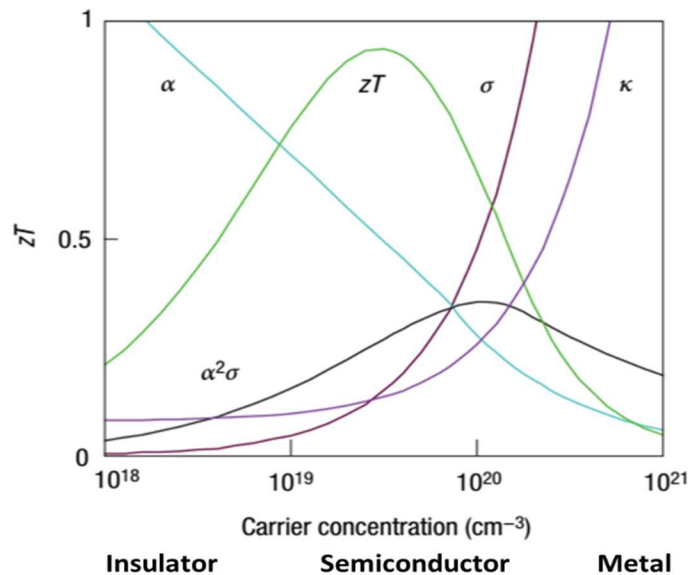


**Figure 1-8 Plot shows the variations in the electrical properties of a thermoelectric material as a function of carrier concentration [11].**



### 1.2.7 Electrical conductivity

Relationship of  $\sigma$  of a semiconductor, carrier concentration and mobility is given below;

$$\sigma = e (\mu_e \cdot n + \mu_h \cdot p) \quad \text{Eq. 1-4}$$

In Eq. 1-4,  $\mu_e$ ,  $n$ ,  $\mu_h$ , and  $p$  are mobility of electrons, density of electrons, mobility of holes, and density of holes, respectively. Change in these parameter leads change in  $\sigma$  of semiconductor. Figure 1-9 shows  $\sigma$  of different materials. Scattering of electrons and holes from lattice and impurity determines mobility. Increase in temperature increase lattice vibrations and hence decrease mobility. Ionized impurities produce crystal defects and effects mobility. At high temperature, impurity scattering decreases and hence mobility increases, which is opposite of lattice scattering. Therefore, type of material, doping, alloying, impurities and temperature influence the  $\sigma$  of TE material. Figure 1-10, shows the effect of  $\sigma$  due to temperature for materials synthesized by hot pressing and spark plasma sintering, material synthesized by SPS showed better  $\sigma$ , may be due to microstructure and density of samples. Structural factors like lattice constant, grain size, and strain also influence  $\sigma$  [8]

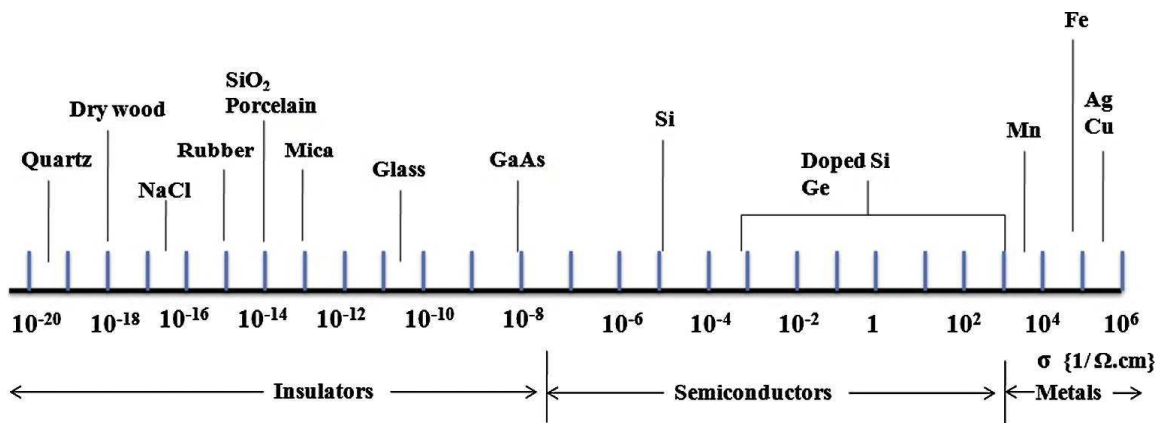


Figure 1-9 Schematic shows the room-temperature electrical conductivity of various materials [12]

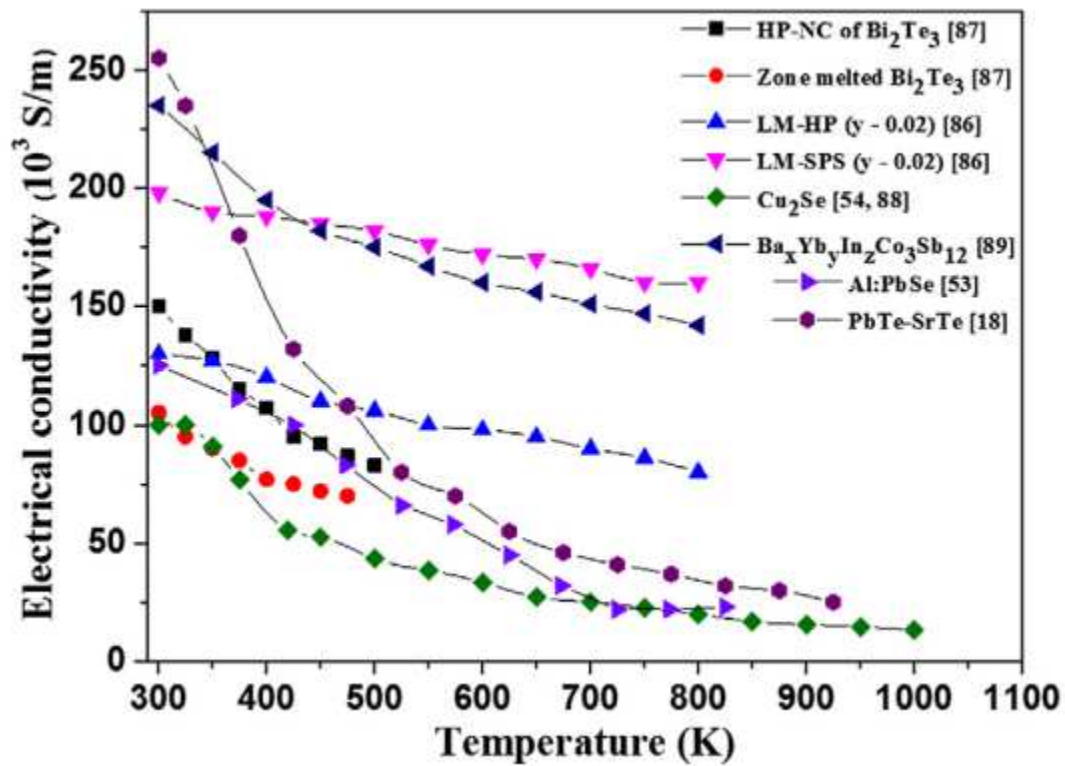


Figure 1-10 Influence of temperature on electrical conductivity of materials synthesized by various methods [8]

## 1.2.8 Thermal conductivity

The total thermal conductivity ( $\kappa$ ) in semiconductors is the sum of two components, one is from charge carriers and other from phonons. Considering one kind of charge is dominant, then total thermal conductivity is the sum of the charge carrier thermal conductivity ( $\kappa_e$ ), and lattice thermal conductivity ( $\kappa_{lat}$ ),  $\kappa = \kappa_{lat} + \kappa_e$ . Increasing  $\kappa_e / \kappa_{lat}$  ratio leads to lower  $\kappa$ , which is possible by decreasing  $\kappa_{lat}$ .  $\kappa$  can be calculated by,  $\kappa = \alpha \cdot C_p \cdot \rho$ , where  $\alpha$  is the thermal diffusivity,  $C_p$  is the specific heat, and  $\rho$  is the density.  $\kappa_e$  can be calculated by Wiedemann–Franz law,  $\kappa_e = L\sigma T$ , where  $L$  is Lorentz constant, which is  $\sim 1.5 \times 10^{-8} \text{ V}^2 \text{ K}^{-2}$  for non-degenerate semiconductors, and  $\sim 2.45 \times 10^{-8} \text{ V}^2 \text{ K}^{-2}$  for metals.  $\kappa_{lat}$  can be calculated by subtracting  $\kappa_e$  from  $\kappa$ ,  $\kappa_{lat} = \kappa - \kappa_e$  [8].

### 1.2.8.1 Slack's model of thermal conductivity

This is simple model and do not consider anharmonic modes but useful in understanding origin of lattice thermal conductivity. Assuming that no optical phonons carry heat and that  $T$  is above  $\theta_D$ , the theoretical lattice thermal conductivity,  $\kappa_{lat}'$  can be expressed by the Eq. 1-5 proposed by Slack [13,14]:

$$\kappa_{lat}' \propto M\delta(\theta_D)^3 / N^{2/3}T \quad \text{Eq. 1-5}$$

where  $M$  is the average atomic mass of the constituent elements,  $\delta^3$  is the average volume occupied by an atom,  $\theta_D$  is the Debye temperature,  $N$  is the number of atoms in the unit cell, and  $T$  is the temperature.

### 1.3 Classification of TE materials

On the basis of maximum  $ZT$ , conventional TE materials can be classified on their working temperatures [15]:

1. Low temperature range ( $<523$  K), for example  $\text{Bi}_2\text{Te}_3$ ,  $\text{Sb}_2\text{Te}_3$
2. Mid temperature range ( $523\text{--}923$  K), for example  $\text{PbTe}$ ,  $\text{Mg}_2\text{Si}$
3. High temperature range ( $>923$  K), for example  $\text{SiGe}$ ,  $\beta\text{-Cu}_2\text{Se}$

#### 1.3.1 Silicide TE materials

Many TE materials developed to date are composed of toxic elements and many are less abundant in earth, for example bismuth-Bi, silver-Ag, antimony-Sb, gallium-Ga, germanium-Ge, selenium-Se, ytterbium-Yb, and tellurium-Te. In contrast, majority of metal silicides are environmental friendly and several are very abundant in earth like  $\beta\text{-FeSi}_2$ ,  $\text{MnSi}_x$ ,  $\text{CrSi}_2$ , and  $\text{Mg}_2\text{Si}$ . High  $S$  has been achieved in transition metal silicides due to their d-band states. Owing to proper melting temperature and band gap, metal silicides are suitable for medium temperature applications,  $500\text{--}800$  K. Thermoelectricity is searching new applications at the present time. Besides high  $ZT$ , materials should be environment friendly, chemical and mechanical strength, cheap, and easily available. Silicon is fourth abundant element in earth core [16,17]. Figure 1-11 shows the cost of different TE materials on the basis of raw materials cost.

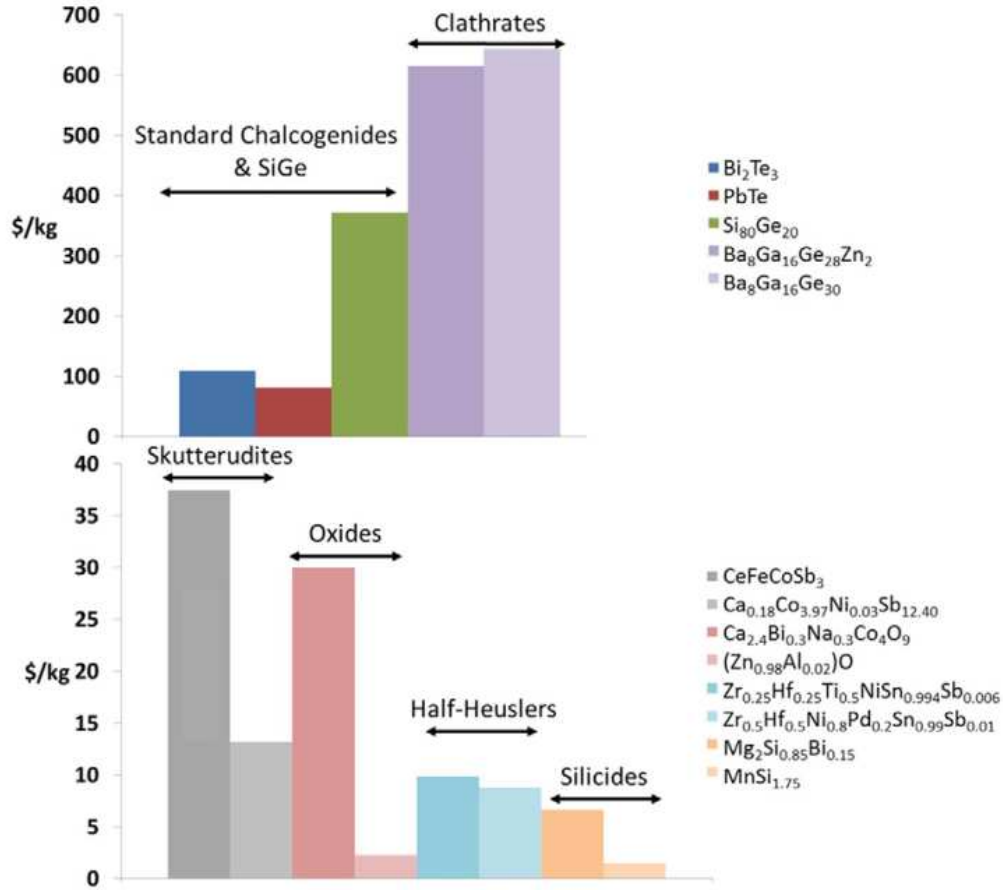


Figure 1-11 Cost of various thermoelectric materials based on the raw material costs of the constituent elements [18].

### 1.3.1.1 Metal silicides

Silicides with transition metals having d-orbitals show unique transport properties and bonding as compared to compounds having s- and p- bonding, resulting in high  $S$  of 150-200  $\mu\text{V/K}$  like  $\text{MnSi}_x$  and  $\beta\text{-FeSi}_2$ . Group IA and IIA silicides are mostly semiconductors, they can easily oxidize owing to chemical reaction and need unusual care. Metal silicides can be classified into groups as below [16];

**Group IA and IIA:** These silicides are generally semiconductors having band gaps ranging from 0.5 to 1.3 eV, including NaSi, Mg<sub>2</sub>Si, Ca<sub>2</sub>Si, BaSi<sub>2</sub>, Sr<sub>2</sub>Si, and SrSi<sub>2</sub> (semi-metal). Due to oxidation problem, these compounds need special care during handling.

**Group III B and rare earth (Sc, Y, and La–Lu):** Except semiconducting ( $\alpha$ -LaSi<sub>2</sub>), these silicides are generally metallic.

**Group IVB (Ti, Zr, and Hf):** These silicides are metallic.

**Group VB (V, Nb, and Ta):** These silicides are metallic.

**Group VIB (Cr, Mo, and W):** These silicides are semiconductors, prospective candidate for TE materials.

**Group VIIB (Mn and Re):** These silicides are semiconductors, extensively used in TE applications.

**Group VIIIB (Fe, Ru, and Os):** These silicides are semiconductors.  $\beta$ -FeSi<sub>2</sub> is low-priced silicide. Theoretically at high temperature Ru<sub>2</sub>Si<sub>3</sub> can be a better TE material than SiGe. Owing to unavailability of suitable dopants and shortage of Ru resources Ru<sub>2</sub>Si<sub>3</sub> cannot be used.

**Group IXB (Co, Rh, and Ir):** These silicides are not good as TE materials

**Group XB (Ni, Pd, and Pt):** These silicides are all metallic.

**Group XIB (Cu, Ag, and Au):** These silicides are not good as TE materials.

**Group XIIB (Zn, Cd, and Hg):** These silicides are not good as TE materials because Zn, Cd, and Hg are less soluble in Si.

Table 1-1 shows some parameters of metal silicides which are used in TE devices. Highest  $ZT$  is attained by solid solution of  $Mg_2(Si,Sn)$  and manganese silicide.

**Table 1-1 Some parameters of silicide materials, which could be used in thermoelectric devices [17].**

Compound	$T_{\text{melting}}$ (K)	Type	$E_g$ (eV)	$ZT_{\text{max}}$	Ref.
$Mg_2Si$	1358	n	0.7	0.9	3
$Mg_2Si-Mg_2Sn$	>1023	n, p	0.4–0.7	1.4 (n) 0.5 (p)	4 5
$Mn_4Si_7$	1430	p	0.66	0.9	6
$ReSi_{1.75}$	2213	p	0.15	0.8	7, 8
$Ru_2Si_3$	1970	n, p	1.1	0.4 (n) 0.2 (p)	9 10
$CrSi_2$	1763	p	0.4–0.7	0.25	11
$FeSi_2$	1490	n, p	0.87	0.4 (n) 0.2 (p)	12 12

### 1.3.1.2 Alkaline earth silicides

#### 1.3.1.2.1 Magnesium silicide ( $Mg_2Si$ ) alloys

As melting point of  $Mg_2Si$  (1358 K) and boiling point of Mg (1363 K) are close, as a result arc melting cannot be used for synthesis of  $Mg_2Si$  [19]. Consequently, other methods like SPS, combustion methods, mechanochemical sintering, ball-milling, hydrogen synthesis are used. Moreover, poor control on composition owing to high vapor pressure of  $Mg_2Si$  and high reactivity of Mg. This results in defects and vacancies and can influence mobility and carrier concentration [20].

At 300 K,  $\text{Mg}_2\text{Si}$  has an indirect band gap of 0.61 eV [21].  $\text{Mg}_2\text{Si}$  was considered as good TE candidate materials for nanostructuring, owing to low  $\kappa$  and high  $S$ .  $\text{Mg}_2\text{Si}$  and  $\text{CaMgSi}$  are expected to be good TE materials because they are composed of earth abundant and environmental friendly elements, low density, and adjustable electronic structure. In the beginning, it was thought that nanostructuring can enhance  $ZT$  of  $\text{Mg}_2\text{Si}$ . Unlike  $\text{SiGe}$ , nanostructuring decreased  $\kappa_{\text{lat}}$  and  $\sigma$ ,  $\sigma$  decreased due to reduction in mobility. Consequently,  $ZT$  could not be increased significantly by nanostructuring. This paved the way to use other strategies like doping, alloying and band structure engineering [16].

Wei Liu et. al [22] reported 15% increase in the power factor in  $\text{Mg}_{2.16}\text{Si}_{0.4}\text{Sn}_{0.6}$  with Bi doping.  $\kappa_{\text{lat}}$  was reduced owing to point scattering. Bi increased electron concentration, as a result  $\sigma$  was 1–2 orders of magnitude higher.  $ZT$  of 1.4 was attained at 800 K. Figure 1-12 shows temperature dependence of TE properties.

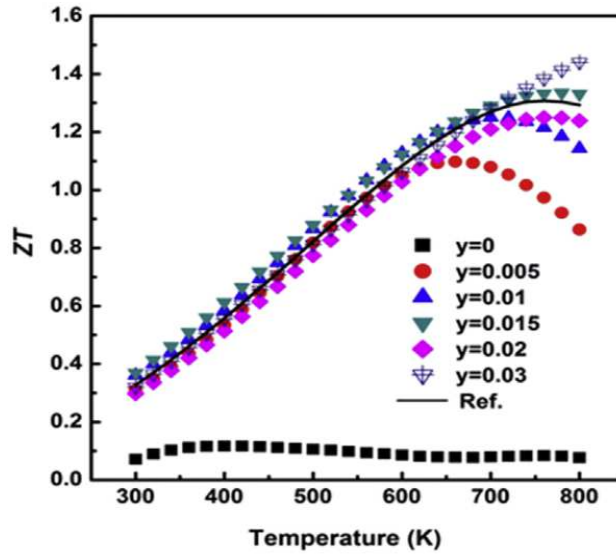


**Figure 1-12 Temperature dependence of TE properties with Bi doping concentration [22]**



### 1.3.1.2.2 Calcium silicide (CaSi, Ca<sub>2</sub>Si, and Ca<sub>5</sub>Si<sub>3</sub>)

Calcium silicides has more than one stable phases at ambient temperature. Among them, Ca<sub>2</sub>Si, is semiconductor, and Ca<sub>5</sub>Si<sub>3</sub> and CaSi are metal. According to pseudopotential calculations, Ca<sub>2</sub>Si is narrow gap semiconductor (0.36 eV) which makes it potential candidate as TE material. Figure 1-13 shows TE properties of Ca<sub>5</sub>Si<sub>3</sub>, and CaSi phases [23].  $\sigma$  reduces with increasing temperature, indicating metallic behavior.  $\sigma$  for Ca<sub>5</sub>Si<sub>3</sub>, and CaSi at 320 K were 2128 S/cm, and 4000 S/cm, respectively.  $S$  sign changes from positive to negative, indicating majority carriers from holes to electrons at high temperature in CaSi, while majority carriers remains same in Ca<sub>5</sub>Si<sub>3</sub> for all temperatures. The ratio of electronic to lattice thermal conductivity reaches about 50% at high temperature. In both samples lattice thermal conductivity reduces proportionally to  $T^{-1}$  showing phonon-phonon scattering in the temperature range.  $\kappa_{\text{lat}}$  reaches 2.1 W/mK, and 2.5 W/mK for Ca<sub>5</sub>Si<sub>3</sub> and CaSi, respectively, at 970 K. Table 1-2 shows some of important properties of silicides.

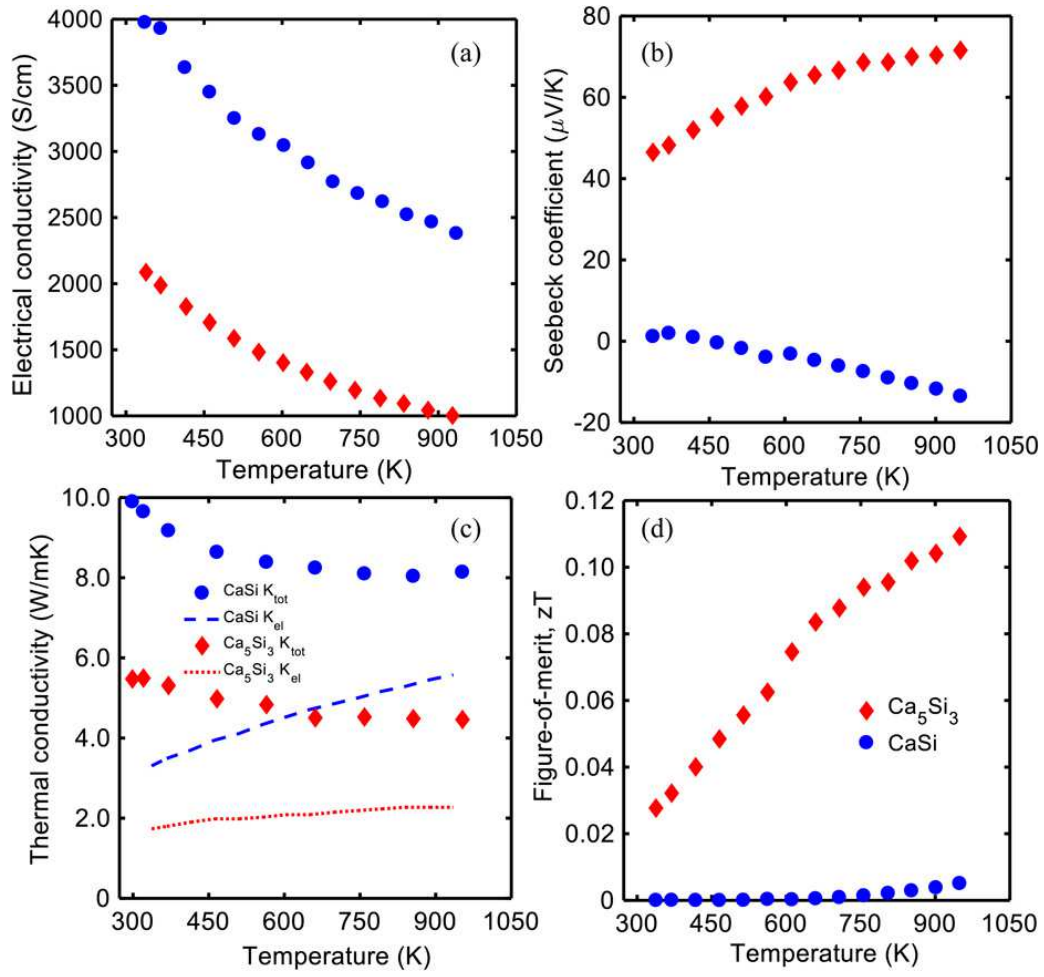


**Figure 1-13 Temperature dependence of TE properties of  $\text{CaSi}$  and  $\text{Ca}_5\text{Si}_3$  (a) electrical conductivity, (b) seebeck coefficient, (c) thermal conductivity, and (d)  $ZT$  [23]**

Table 1-2 List of main properties of silicides [16]

Material	Type (n or p)	Lattice structure	Density (g/cm <sup>3</sup> )	Melting point (°C)	Bandgap (eV)	$\kappa$ at max. $zT$ (W m <sup>-1</sup> K <sup>-1</sup> )	Max. $zT$	Temp. at max. $zT$ (K)	Ref. <sup>a)</sup>
Mg <sub>2</sub> Si	(n)	Cubic	1.99	1102	0.61–0.67	2.9	0.5–0.6	850	108, 107, 104
Mg <sub>2</sub> Si	(p)	Cubic	1.96	1102	0.61–0.67	2.2	0.11	650	104, 111
Mg <sub>2</sub> (Si,Sn)	(n)	Cubic	—	800	—	2.3	1.3	700	106
Mg <sub>2</sub> (Si,Sn)	(p)	Cubic	—	800	—	2.5	0.5	750	109
Mg <sub>2</sub> SiGe	(p)	Cubic	2.42	—	0.68	1.7	0.36	625	111
Mg <sub>2</sub> SiGe	(n)	Cubic	1.97	—	—	2.4	0.74	756	108
MnSi <sub>4</sub>	(p)	Tetragonal	5.186–5.23	1156.85	0.4–0.7	2.8–3.8	0.5–0.6	800	120, 82
Si <sub>1-x</sub> Ge <sub>x</sub> <sup>b)</sup>	(p)	Diamond	2.329–5.323	937–1412	0.66–1.12	2.39	0.95	1173	46, 44, 206
Si <sub>1-x</sub> Ge <sub>x</sub> <sup>b)</sup>	(n)	Diamond	2.329–5.323	937–1412	0.66–1.12	1.97–2.7	1.2–1.3	1073–1223	36, 37, 47
ReSi <sub>2</sub>	(p)	Tetragonal	10.78	1977	0.12	—	—	—	—
ReSi <sub>1.75</sub>	(p)	Triclinic	—	1940	0.16	4.6	0.7	1060	144
Ru <sub>2</sub> Si <sub>3</sub>	(n)	Orthorhombic	6.96	1697	0.8–1.1	2.2	0.2	900	146
URu <sub>2</sub> Si <sub>2</sub>	(p)	Tetragonal	—	~1800	0.1	~2.3	0.1	1082	147
USi <sub>3</sub>	(p)	Cubic	—	~1600	—	~9	~0.3	1173	148
Os <sub>2</sub> Si <sub>3</sub>	(p)	Orthorhombic	11.15	—	2.3	—	—	—	—
Ir <sub>3</sub> Si <sub>5</sub>	(p)	Monoclinic	10.12	1400	1.2	—	~0.3	1100	151
CrSi <sub>2</sub>	(p)	Hexagonal	4.98	1470	0.32–0.35	12.1	0.25	980	137, 139
$\alpha$ -FeSi <sub>2</sub>	(p)	Tetragonal	4.99	1217	Metallic	—	—	—	—
$\beta$ -FeSi <sub>2</sub>	(p)	Orthorhombic	4.93	Stable <928	0.7–0.95	4.6	0.25	750	165
$\beta$ -FeSi <sub>2</sub>	(n)	Orthorhombic	4.93	Stable <928	0.7–0.95	3.4–3.6	0.5	890–1050	85
CoSi	(p)	Cubic	6.58	1450	–0.041	11	0.04	300	173
CoSi	(n)	Cubic	6.58	1450	–0.041	14	0.35	400	175
CoSi <sub>1-x</sub> Ge <sub>x</sub>	(n)	Cubic	6.58	1450	—	10.5	0.1	350	179
SrAl <sub>2</sub> Si <sub>2</sub>	(n), (p)	Hexagonal	2.924	1020	~0.02	~55	0.034	381	199
BaSi <sub>2</sub>	(n)	Orthorhombic	3.54–3.68	1180	1.13–1.30	0.6	0.07	950	204
SrSi <sub>2</sub>	(n)	Cubic	3.35	1100	0.013–0.035	~5.5	0.4	300	193, 207
CaSi	(n)	Orthorhombic	2.31	1324	—	2.5	5.1 × 10 <sup>-3</sup>	950	205
Ca <sub>5</sub> Si <sub>3</sub>	(p)	Tetragonal	—	—	—	2.1	0.11	950	205
CaSi <sub>2</sub>		Cubic	2.5	1020	0.36	—	—	—	—
MoSi <sub>2</sub>	(p)	Body-centered tetragonal	6.28	~2030	—	48.5	—	—	—
$\beta$ -MoSi <sub>2</sub>	(p)	Hexagonal	6.32	~1900	0.07	—	—	—	—
$\beta$ -MoSi <sub>2</sub>	(n)	Hexagonal	6.32	~1900	0.07	—	—	—	—
WSi <sub>2</sub>	(p)	Hexagonal	9.88	~2160	0.07	—	—	—	—
CeSi <sub>2</sub>	(n)	Tetragonal	5.31	1620	—	12.6	0.085	240	183
LaSi	(n)	Orthorhombic	—	1620	0.19	6.71	0.002	957	53, 194

a) The listed references are for the thermal conductivity and  $zT$  values. The references for some other material properties are Refs. 208, 209, and 210.

b) Density (g/cm<sup>3</sup>):  $2.329 + 3.493x - 0.499x^2$ , Melting point (°C):  $1412 - 738x + 263x^2$  (solidus) and  $1412 - 80x - 395x^2$  (liquidus), Bandgap (eV): for  $x < 0.85$ :  $1.12 - 0.41x + 0.008x^2$  for  $x > 0.85$ :  $1.86 - 1.2x$ .

## 1.4 Effect of Humidity and Oxide on TE properties of Mg<sub>2</sub>Si

Due to volatilization and oxidation of Mg, it is difficult to get good quality samples of Mg<sub>2</sub>Si. Fusion synthesis techniques are used to improve structure, composition and quality of Mg<sub>2</sub>Si to reduce effect of volatilization and oxidation. Difference in melting temperature of Mg and Si can have affect as well. Therefore, SPS technique is used to reduce oxidation due to high diffusion velocity at lower temperature [24].

Y. Mito et al. studied humidity and oxidation of Mg<sub>2</sub>Si [25]. Mg<sub>2</sub>Si powder was exposed to high humidity at room temperature, which was expected to absorb on surface. At high temperature during SPS, Mg<sub>2</sub>Si can react with moisture according to the reaction given in Eq. 1-6, resulting in formation of MgO and SiH<sub>4</sub>. This can reduce density of samples and crystallinity. Figure 1-14 shows the XRD results of samples exposed to different percentage of humidity. Samples exposed to higher levels of humidity shows higher MgO.

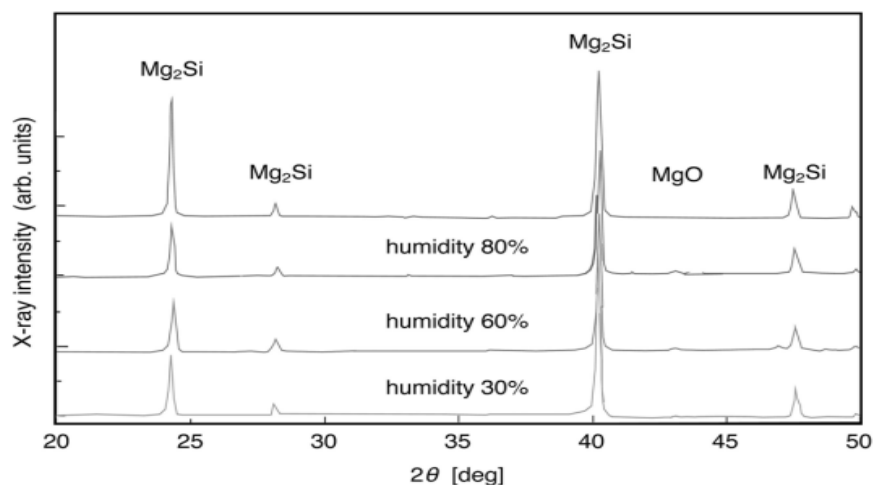


**Figure 1-14 Powder XRD diffraction patterns of the Sb-doped Mg<sub>2</sub>Si TE-legs fabricated by SPS using raw material powders exposed to atmosphere with the humidity of 30, 60, and 80% for 24 hours [25]**

Figure 1-15 shows the thermograms of TG and DTA of  $\text{Mg}_2\text{Si}$  samples having 0 and 4 wt. %  $\text{MgO}$ , which were obtained by exposing powder to humidity. The purpose was to study effect of oxidation. Both samples shows same behavior, which indicates samples having small amount of  $\text{MgO}$  will not affect oxidation reaction. DTA results shows three exothermic peaks, peak about 550 °C can be due to oxidation because weight increases rapidly in TG after 500 °C. Oxidation of  $\text{Mg}_2\text{Si}$  can be given by the reaction shown in Eq. 1-7;

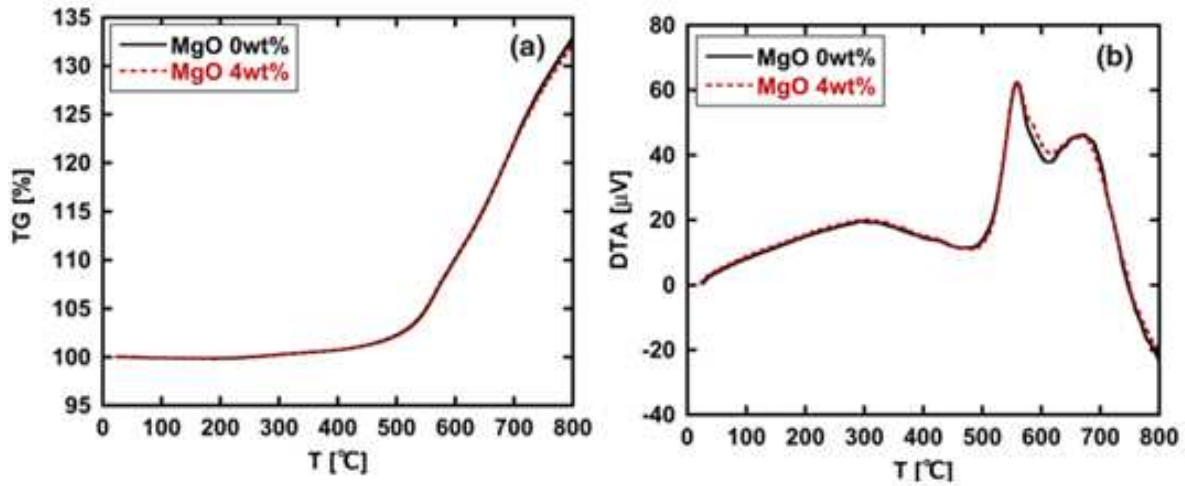


**Figure 1-15 Thermograms of TG (a) and DTA; (b) analysis of  $\text{Mg}_2\text{Si}$  samples containing 0 wt.%, and 4 wt.%  $\text{MgO}$  [25].**

S. Fiameni et al. reported the effect on crystallize size and  $\text{MgO}$  content by ball milling, thermal treatment and electrical measurement in Bi doped of  $\text{Mg}_2\text{Si}$  [26]. XRD analysis was performed after sample preparation and electrical measurement for all samples. Effect of doping was not significant on size of crystallite. Therefore, XRD analysis was carried out for the best sample with Bi,  $x = 0.02$ , Figure 1-16 (a). The crystallite size increased for each step during synthesis (ball milling, thermal treatment (TT), spark plasma sintering (SPS)), laser flash measurements/analysis

(LFA), and electrical measurement/analysis (EA). Such behavior pointed out limitations of maintaining the original crystallite size in silicides. Furthermore, the amount of oxide (MgO) was increased after thermal treatment and SPS, as shown in Figure 1-16 (b). Oxide effected Seebeck coefficient insignificantly, thermal conductivity slightly increased and electrical resistivity increased significantly and was higher than previous studies.

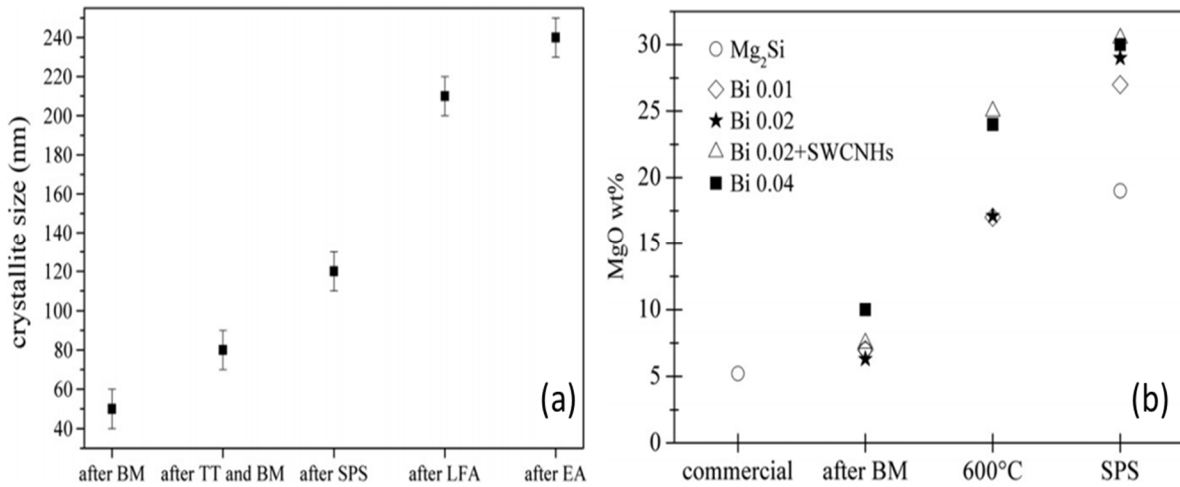


**Figure 1-16 (a) Crystallite size trend after each synthesis process and after functional analyses, and (b) MgO amount in the commercial material and after the different thermal processes [26].**

## 1.5 Composite Effect

### 1.5.1 Nanostructures, and Nanostructure bulk materials

For many decades  $ZT$  value remained below 1. With the nanotechnology,  $ZT > 1$  was made possible. Nanostructures and nanocomposites research helped in improving  $ZT$  by separating the interrelated properties ( $S$ ,  $\sigma$  and  $\kappa$ ) of TE materials. Exact mechanism of enhancement in properties is still not clear. The results of nanostructuring depends upon kind of nanotstructure and synthesis process [27].

Figure 1-17 shows schematic illustration of strategies to enhance TE performance of materials by changing their structures from macro- to nanoscale. These are divided into two approaches: 1) First approach is decreasing dimension of bulk to smaller dimension where quantum size and interface effects, as shown in Figure 1-17 (a)-(d). Venkatasubramanian et al. reported  $ZT$  value of 2.4 at room temperature for p-type superlattices made of  $\text{Bi}_2\text{Te}_3/\text{Sb}_2\text{Te}_3$  alternating layers [28]. Fabrication of superlattices by chemical or physical vapor deposition techniques are expensive and not suitable for bulk applications.

2) Second approach is the formation nanostructured bulk materials which are bulk materials composed of nanostructured features, as shown in Figure 1-17 (e)-(j). These materials are cheaper and easier to attain same  $ZT$  enhancements as for nano dimension bulk materials (approach 1). In most systems, such enhancement is due to decrease in  $\kappa_{\text{lat}}$  due to high density of interfaces. Rowe et al. [29] reported for the first time that 20 % reduction in  $\kappa$  is possible if grain size of alloy reduced by few microns. Later on, with advancement in fabrication and characterization techniques, nanoscale features got more attraction in field of thermoelectricity.

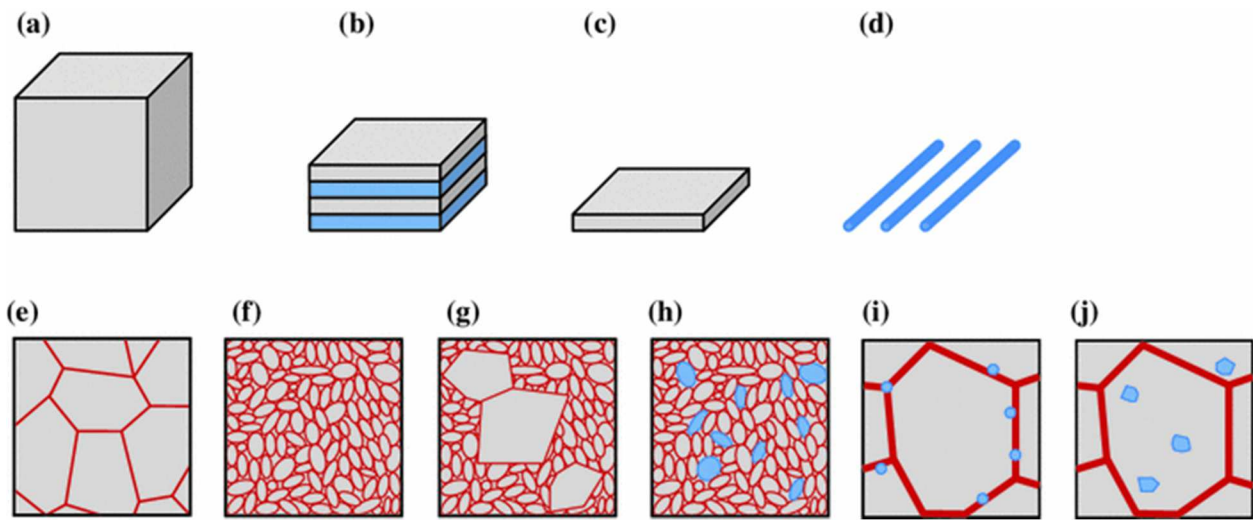


**Figure 1-17** Schematic illustration of general strategies for improving thermoelectric performance of materials by modifying the structures from macro- to nanoscale. a–d Change in dimensionality and size: a bulk, b superlattice, c thin-film, d nanowires; e–h Modification of the grain structures in bulk: e micrometer grains, f nanometer grains, g mixture of grains with different sizes, h mixture of nanoparticles with different compositions; i–j Composites of embedded nanoparticles in a bulk matrix, formed by: i co-compaction of a physical mixture of the two components, j in situ formation of nanosize precipitates within the bulk matrix [27].



## 1.5.2 Mechanisms for improving TE materials by introduction of nanoparticles

### 1.5.2.1 Alloying

Alloying is traditional way for lowering  $\kappa$  to improve TE properties. Short wavelength phonons scatters from substituting atoms acting as point defects. Scattering depends upon mass, and bond stiffness but it is more effective if it exist in dispersed fashion. At low temperature, alloying can reduce  $\kappa$ , while maintaining good  $\sigma$  [30,31]. Introducing nanoparticles of different material in bulk can reduce  $\kappa$  further. In order to avoid reduction of  $\sigma$  selection of appropriate nanoparticle is important. Some of the factors important for choosing nanoparticles are lattice mismatch, potential barrier on interface between nanoparticles and bulk material. Difference in atomic mass and bond stiffness can increase scattering. Size of particle can also have effect on scattering efficiency [32–34]. Figure 1-18 shows phonon scattering of various mean free path [15].

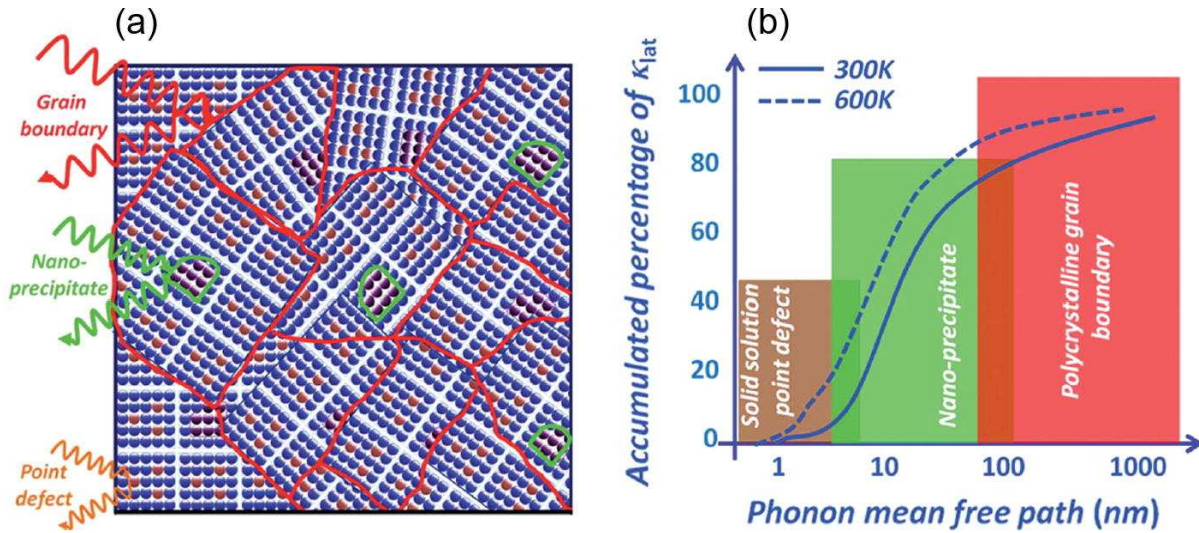


**Figure 1-18 (a) All-scale hierarchical architectures exhibiting the scattering of phonons of different mean free paths and (b) cumulative distribution function of lattice thermal conductivity with respect to the phonon mean free path in Si or PbTe bulk [15].**

### 1.5.2.2 Energy filtering

With efforts for reducing  $\kappa$  by nanoinclusions, researchers also studied the electron transport properties of nanocomposites. The relatively new idea was put forward to enhance power factor [27]. The concept of energy filtering was first studied in plane for superlattices, then for nanodot heterostructures. The main idea of this theory is the filtering of electrons, low energy electrons scatter and high energy electron dominates transport. This concept was reported in indium gallium arsenide superlattice [35], and bulk lead telluride with lead nanoinclusions [36].

S. V. Faleev et al. [37] reported the theory for enhancement of TE properties in semiconductors by metallic nanoinclusions, representing band bending on semiconductor/metal boundary acting as energy filter of electrons. As a result  $S$  increases significantly due to energy dependent electronic scattering time. The main idea of this concept is shown in Figure 1-19. Spherical metal particle having radius  $R$  and volume fraction  $x$  are haphazardly distributed in bulk semiconductor. On metal/semiconductor boundary, charge transfer between metal and semiconductor, resulting in band bending away from boundary, given by electrostatic potential  $V(r)$ , Figure 1-19 (b). This potential results in energy-dependent scattering of electrons, as shown in Figure 1-19 (c). Electrons with high energy do not suffer with potential, on the other hand low energy electrons do. Seebeck coefficient relies on energy derivative of relaxation time  $d \ln \tau(E) / dE$  at the Fermi energy. This mechanism can enhance the Seebeck coefficient.

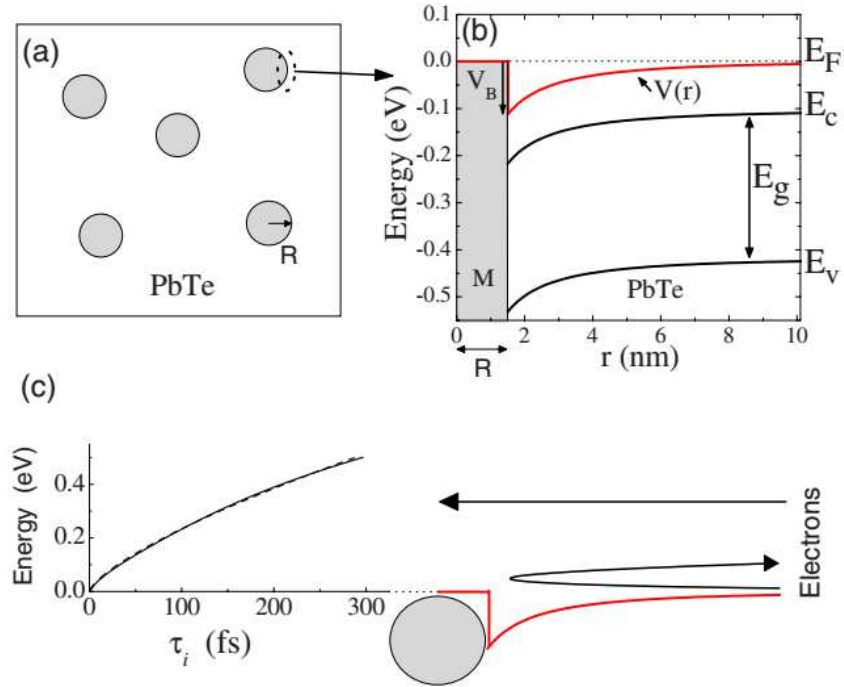


**Figure 1-19 Schematic of the semiconductor host with metallic nanoinclusions. Panel (b) shows an example of the calculated potential  $V(r)$  and the energy diagram for PbTe at  $T = 300$  K,  $n = 2.5 \times 10^{19} \text{ cm}^{-3}$ ,  $V_B = -0.11 \text{ eV}$ , and  $R = 1.5 \text{ nm}$ . Panel (c) illustrates the concept of energy filtering: low energy electrons scatter strongly with the potential, but high energy electrons are unaffected. The calculated electronic relaxation time for the potential of panel (b) is also shown [37].**

## 1.6 Improving $ZT$ by micron size metallic phase

Power factor of higher  $\rho$  materials can be improved by reducing  $\rho$  through introduction of higher electrical conductivity metallic phase. The metallic phase provides conductive paths, which decrease  $\rho$ . Addition of metallic phase can also increase  $\kappa$ , maximum  $ZT$  is possible by optimizing  $\rho$ , and  $\kappa$ . D. Srivastava et al. [38] enhanced  $ZT$  of  $\text{Sr}_{0.8}\text{La}_{0.067}\text{Ti}_{0.8}\text{Nb}_{0.2}\text{O}_{3-\delta}$  ceramic samples by introducing micron size (1–3  $\mu\text{m}$ ) Cu or Fe inclusions. High quality samples with Cu and Fe particles were synthesized by the mixed oxide method, then sintered in reducing conditions at 1700 K. Phase analysis by XRD and microstructural analysis by SEM demonstrated (Figure 1-20) that

the material is mainly made of cubic  $\text{SrTiO}_3$  phase, with rutile-structured minor phases and metallic particles on the grain boundaries.  $\rho$  decreased by 5 times and  $P$  increased by 75%. Both Cu and Fe enhanced  $ZT$ , increasing the  $ZT$  from 0.25 at 1000 K for the control sample, to  $ZT$  of 0.36 at 900 K for the Cu-containing samples and to 0.38 at 1000 K for the Fe-containing samples. Figure 1-21 shows TE properties of all samples.

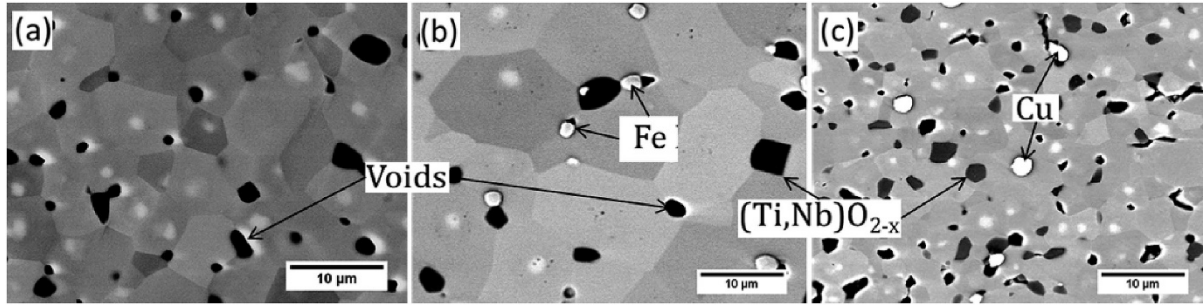


**Figure 1-20 SEM micrographs of  $\text{Sr}_{0.8}\text{La}_{0.06}\text{Ti}_{0.8}\text{Nb}_{0.2}\text{O}_3$  samples: (a) control, (b) prepared with Fe additions, (c) prepared with Cu additions [38].**

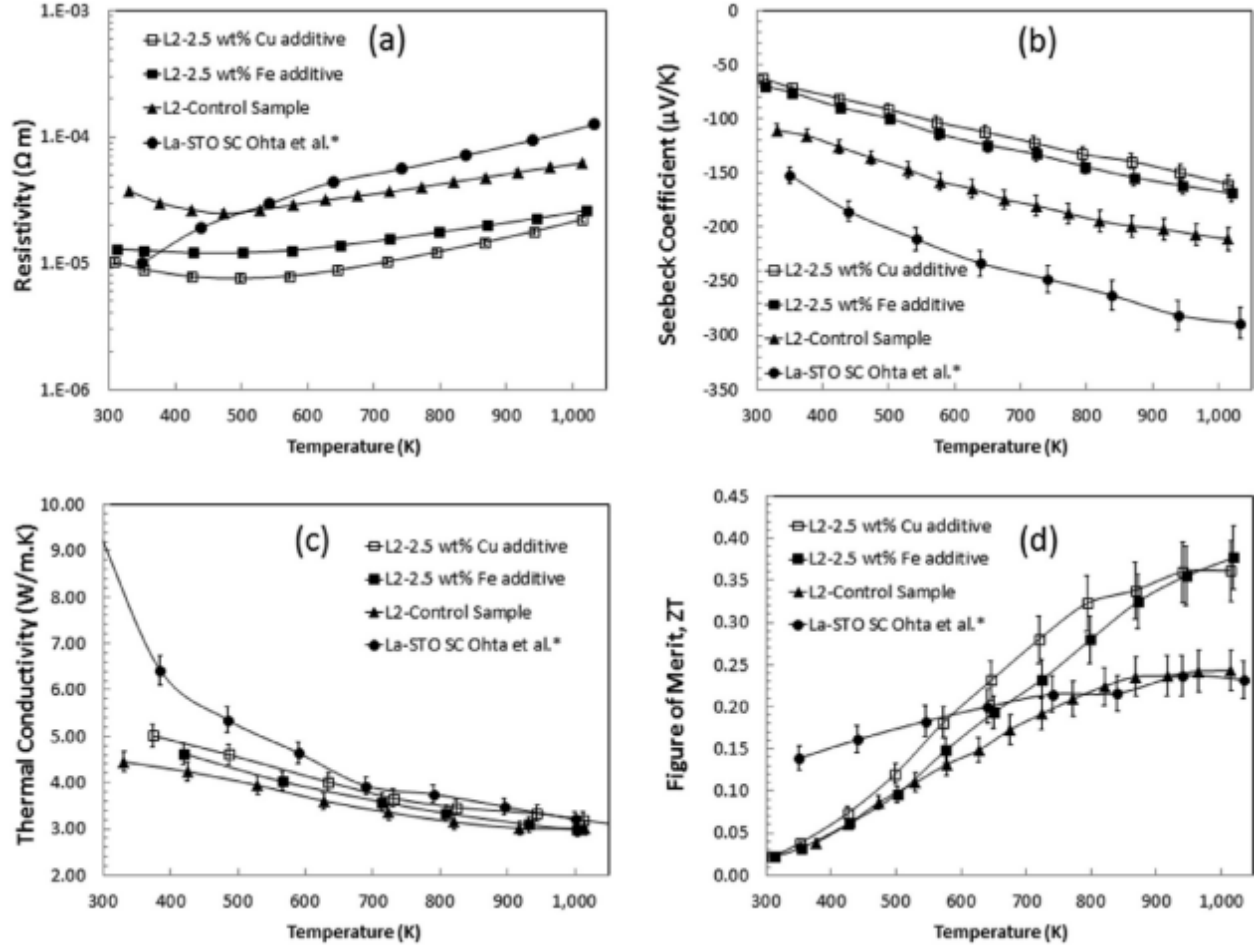
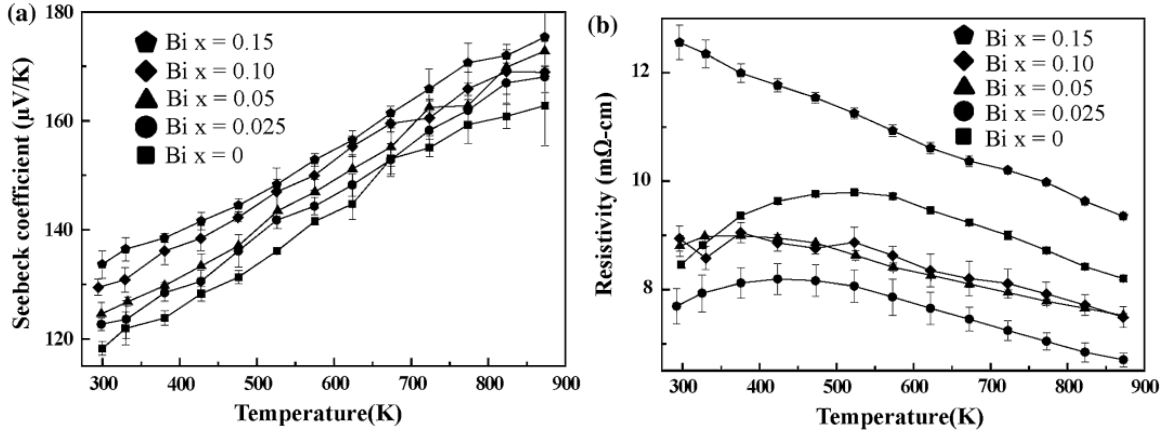


Figure 1-21 Thermoelectric properties of the  $\text{Sr}_{0.8}\text{La}_{0.06}\text{Ti}_{0.8}\text{Nb}_{0.2}\text{O}_3$  (control) and the Cu-containing and Fe-containing samples as a function of temperature: (a) electrical resistivity, (b) Seebeck coefficient, (c) thermal conductivity, (d) figure of merit,  $ZT$ . Data for doped single crystal  $\text{SrTiO}_3$  is from literature for comparison [38].

## 1.7 Simultaneous decrease in electrical resistivity and increase in Seebeck coefficient

$\rho$  can be decreased by increasing carrier concentration and introduction of metallic phase, but this also decreases  $S$ . Simultaneous decrease in  $\rho$  and increase in  $S$  is rare but possible.  $S$  can increase if charge carriers (e.g., electrons) opposite to dominant charge carriers (e.g., holes) increases. Cho. et al. reported simultaneous increase in  $S$  and decrease in  $\rho$  in the study of trivalent Bi doping in

$\text{Ca}_3\text{Co}_4\text{O}_9$  (Ca-349) [39] for specific doping amount, Figure 1-22. Majority carriers were holes so  $S$  was positive. With the addition of Bi doping, majority carriers (holes) decreased, which resulted in increase in  $\rho$  and  $S$ , as shown in Figure 1-22. At  $x = 0.025$ ,  $\rho$  decreased, may be due to the formation of the low electrical conductivity  $\text{Bi}_2\text{O}_3$  on the grain boundary.



**Figure 1-22** Temperature dependence of (a) Seebeck coefficient and (b) electrical resistivity of  $\text{Ca}_3\text{Bi}_x\text{Co}_4\text{O}_9$  with  $x = 0$  to  $0.15$  [39].

T. Mori et al. explained the phenomenon of simultaneous decrease of  $\rho$  and increase in  $S$  in  $\text{YB}_{22}\text{C}_2\text{N}$  [40], clarifying that it was because of hybrid/composite effect, where high conductive channels were partly formed. Simultaneously, it was guessed that intrinsic doping alters the electronic structure of the main phase. Conductive channels lead to lowering  $\rho$  and intrinsic doping lead to increasing  $S$ . As shown in Figure 1-23 (a)-(b) [41], all of the  $\text{VB}_2$  doped/seeded samples showed a very large decrease in  $\rho$  by more than 2 orders, in comparison to the non-doped sample. Moreover, increase in the maximum absolute value of the  $S$  was concurrently witnessed. In case of 16 vol%  $\text{VB}_2$  doped sample, the  $S$  rise is smaller because of large amounts of metallic seeded  $\text{VB}_2$ . After heat treatment of 11 vol%  $\text{VB}_2$ , volume of  $\text{VB}_2$  reduced to 9 vol%, this suggested intrinsic doping of V into  $\text{YB}_{22}\text{C}_2\text{N}$ .

Figure 1-23 (c) shows the elemental mapping of Vanadium (V), showing the hybrid effect which resulted in reduction of  $\rho$ . V is spread like a “nanoweb” finely lying on some grains. From XRD, this V existed as metallic  $\text{VB}_2$ .

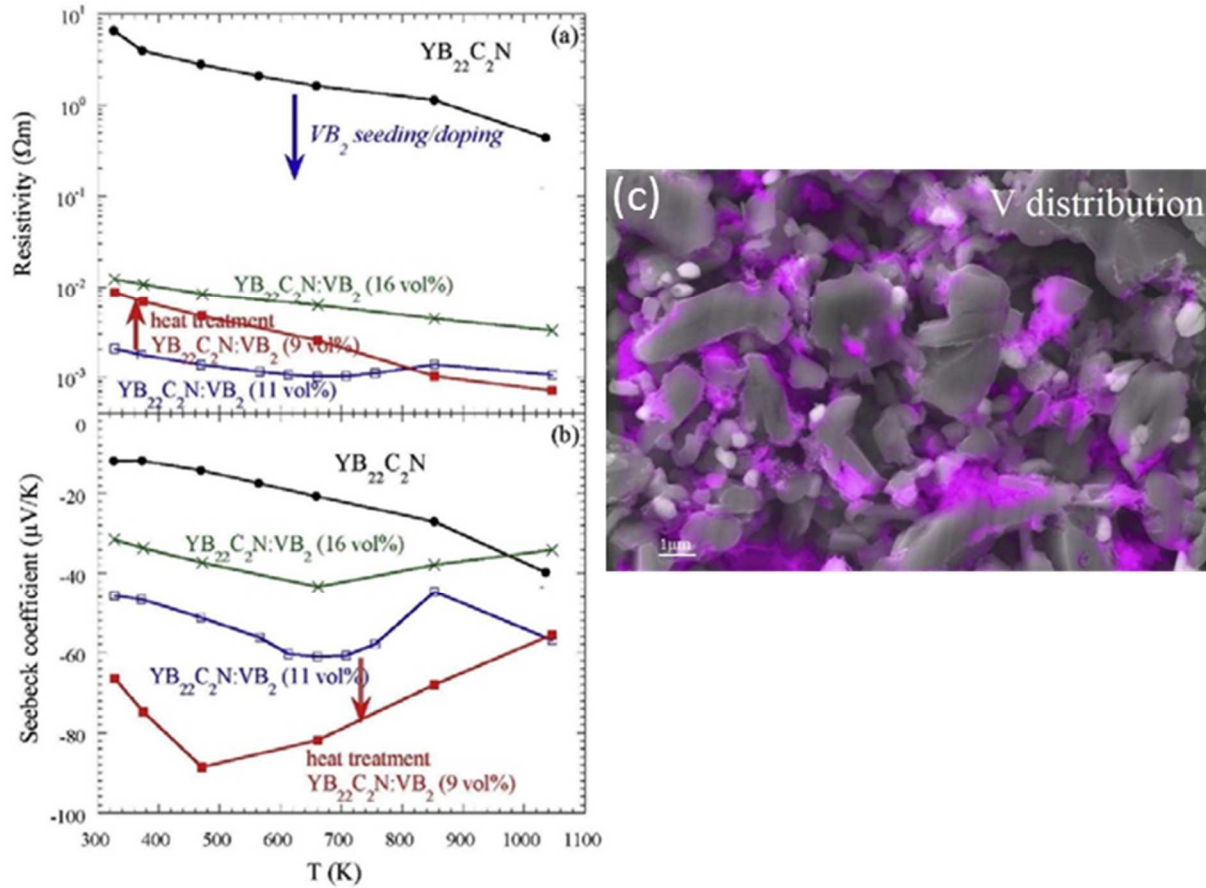


**Figure 1-23 (a) Electrical resistivity and (b) Seebeck coefficient of non-doped  $\text{YB}_{22}\text{C}_2\text{N}$  (●) and  $\text{VB}_2$  doped/seeded  $\text{YB}_{22}\text{C}_2\text{N}$  [41]. Heat treatment changed  $\text{VB}_2$  content 11 vol% (□) to 9 vol% (■) for same sample. Data for a heavily 16 vol% doped/seeded sample with multiple heating (x) is also shown. (c) EDS mapping of V of  $\text{VB}_2$  doped/seeded  $\text{YB}_{22}\text{CN}$ , the heavily 16 vol% doped/seeded sample with multiple heating [40].**

It is obvious developing such samples which demonstrate simultaneous increase in  $S$  and decrease in  $\rho$  is challenging but has potential to achieve high  $ZT$ .

### 3. Strontium silicides ( $\text{Sr}_2\text{Si}$ , $\text{Sr}_5\text{Si}_3$ , and their composites)

#### 3.1 Experimental

Palenzona et al. [45] used strontium and silicon for synthesis of strontium silicide phases for phase diagram study. We used strontium granules (Sigma-Aldrich, 99.9% purity) and strontium disilicide powder (Sigma-Aldrich, 99% purity) to synthesize  $\text{Sr}_2\text{Si}$  powder. Sr and  $\text{SrSi}_2$  were inserted into a titanium tube in an Ar-filled glovebox, where the working atmosphere of the glovebox was continuously purified to values  $<1$  ppm (with respect to  $\text{H}_2\text{O}/\text{O}_2$ ). To compensate for the loss of Sr by evaporation in the atmosphere during synthesis, 5–10% excess Sr was added to samples A–F. The Ti tube was closed by welding in an arc melting furnace under argon (6N) atmosphere. Details of the fabrication process are shown in Table 3-1, which includes the starting composition, synthesis, and SPS conditions. The Ti tube was then sealed in an Ar-filled (0.075 MPa at room temperature) quartz tube and heated in an electric furnace. After this synthesis process, the Ti tube was opened and the agglomerates were pulverized in a glovebox. This powder was consolidated by using a SPS technique (SPS-515 S, Fuji Electronic Industrial Co.) under Ar atmosphere.

After each process, powder X-ray diffraction (XRD) analysis with Cu  $K\alpha$  radiation (Smart Lab, Rigaku Co.) was carried out. To avoid exposure of the samples to air during the XRD, each sample was covered by a half-cylindrical aluminum holder with a window of Kapton film.  $S$  and  $\rho$  were measured in He atmosphere (0.04 MPa at room temperature) by using ZEM-1 (ULVAC, RIKO Co.), which employs a steady-state temperature gradient and four-probe method.  $\kappa$  was obtained by measuring the geometric density, estimating the specific heat by the Dulong–Petit law, and



measuring the thermal diffusivity using the laser flash method (TC-7000, ULVAC-RIKO Co.). The transverse and longitudinal speeds of sound were measured using an ultrasonic pulse echo method (Echomer 1062, Nihon Matech Co.). The phases and relative densities (relative to  $\text{Sr}_2\text{Si}$ ) of the samples after SPS are given in Table 3-2.

**Table 3-1 Sample details for all samples, where the SPS time is the time at maximum temperature, where h is hour.**

Sample Name	Starting Composition	Synthesis		SPS		
		T (K)	t (h)	T (K)	P (MPa)	t (min)
A	$\text{Sr}_{2.150}\text{Si}$	1250	48	698	672	14
B	$\text{Sr}_{2.075}\text{Si}$			953	115	8
C	$\text{Sr}_{2.150}\text{Si}$					16
D	$\text{Sr}_{2.075}\text{Si}$					6
E	$\text{Sr}_{2.150}\text{Si}$					19
F	$\text{Sr}_{2.113}\text{Si}$					17
G	$\text{Sr}_{2.113}\text{Si}$					60
H	$\text{Sr}_5\text{Si}_3$			1225		12

**Table 3-2 Phases and relative densities after SPS, relative density is with respect to  $\text{Sr}_2\text{Si}$  phase.**

Sample Name	Main Phase	Secondary Phases	Relative Density
A	$\text{Sr}_2\text{Si}$	$\text{Sr}_3\text{SiO}$	92
B	$\text{Sr}_2\text{Si}$	$\text{Sr}_3\text{SiO}$	99
C	$\text{Sr}_2\text{Si}$	$\text{Sr}_5\text{Si}_3$ , $\text{Sr}_3\text{SiO}$	100
D	$\text{Sr}_2\text{Si}$	$\text{Sr}_5\text{Si}_3$ , $\text{Sr}_3\text{SiO}$	100
E	$\text{Sr}_2\text{Si}$	$\text{Sr}_5\text{Si}_3$ , $\text{Sr}_3\text{SiO}$	101
F	$\text{Sr}_2\text{Si}$	$\text{Sr}_5\text{Si}_3$ , $\text{Sr}_3\text{SiO}$	102
G	$\text{Sr}_2\text{Si}$	$\text{Sr}_5\text{Si}_3$ , $\text{Sr}_3\text{SiO}$	103
H	$\text{Sr}_5\text{Si}_3$	$\text{Sr}_3\text{SiO}$	96

## 3.2 Results

### 3.2.1 Phase analysis

#### 3.2.1.1 After synthesis

The XRD patterns of all samples after synthesis are given in Fig. 3-1. The synthesis powder conditions were same for all samples. After synthesis,  $\text{Sr}_2\text{Si}$  and  $\text{Sr}_5\text{Si}_3$  were successfully obtained as the main phase in samples A–F and sample G, respectively, with minor amounts of  $\text{Sr}_3\text{SiO}$  impurity in all samples and  $\text{SrSi}$  in sample G.  $\text{Sr}_5\text{Si}_3$  was successfully introduced in samples C–F as a secondary phase during SPS.  $\text{Sr}_5\text{Si}_3$  crystallized in a tetragonal,  $\text{Sr}_5\text{Si}_3$ -type structure [space group:  $I4cm$  (108)], and  $\text{Sr}_3\text{SiO}$  crystallized in an orthorhombic, anti-perovskite structure [space group:  $Pbnm$  (62)]. Samples with  $\text{Sr}_2\text{Si}$  as the main phase could not be obtained without adding excess Sr. An excess of 5–10% Sr was added to samples A–F to compensate for the loss of Sr.

However, no clear effect on changing the amount of excess Sr from 5 to 10% was observed in the XRD patterns after synthesis, as shown in Figure 3-1.

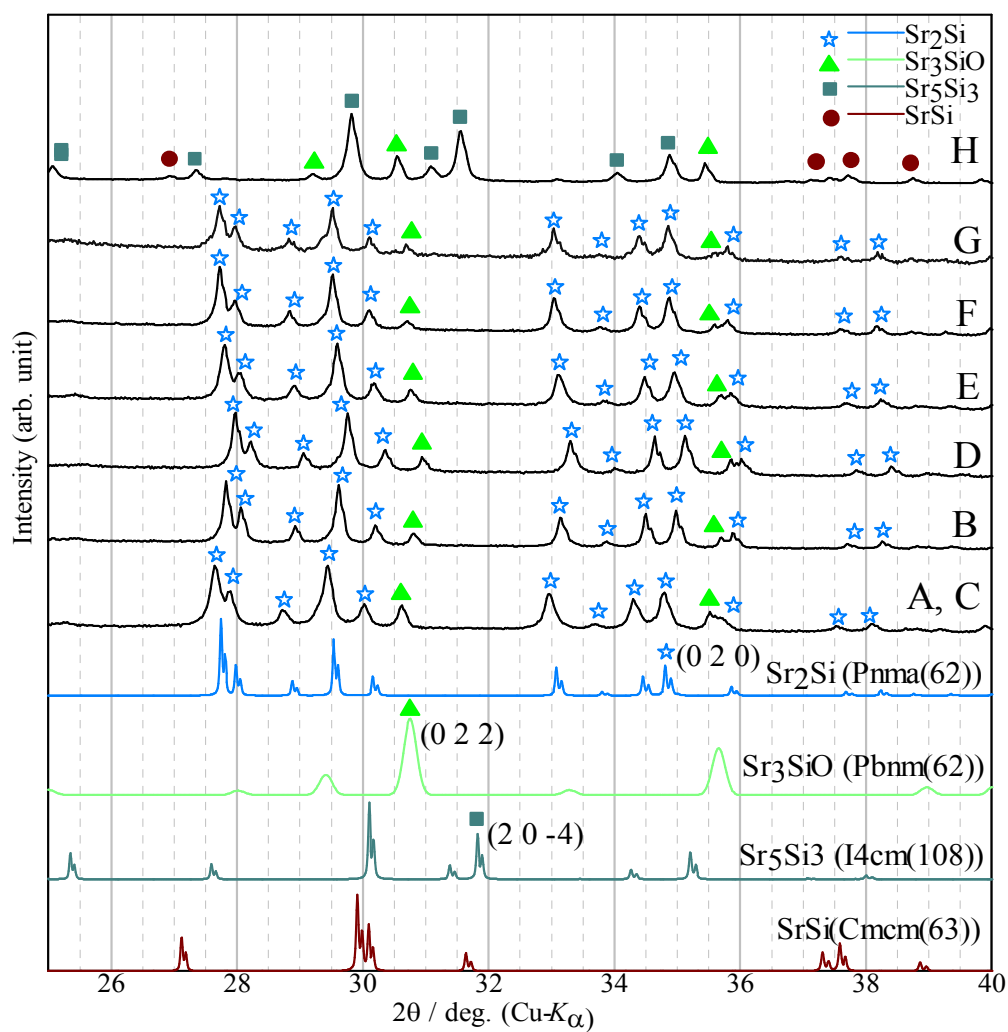


**Figure 3-1 XRD patterns of all samples after synthesis**

### 3.2.1.2 After SPS

The XRD patterns of all samples after SPS are in Figure 3-2. We synthesized three kinds of samples in this work: (1) main phase is  $\text{Sr}_2\text{Si}$  (sample A), (2) main phase is  $\text{Sr}_5\text{Si}_3$  (sample H), and (3) composites of  $\text{Sr}_2\text{Si}$  and  $\text{Sr}_5\text{Si}_3$ , main phase is  $\text{Sr}_2\text{Si}$  (samples C–G). The synthesis conditions for all samples A–H were the same. Depending upon the main phase of the samples, the SPS conditions were different. SPS conditions were same for all composite samples C–F except composite sample G. In samples C–F, the time at maximum sintering temperature slightly varied depending upon when sintering was finished. The purpose of varying the SPS time was to obtain dense samples for the investigation of the TE properties. The SPS temperature, pressure, and time at maximum temperature controlled the phase transformation, density, and density, respectively. In composite sample G, SPS temperature was same as composite samples C–F but time was deliberately increased to 60 minutes, in order to study the effect on amount of  $\text{Sr}_5\text{Si}_3$  phase and thermoelectric properties.

The SPS temperatures for samples A, B–G, and H were 698 K, 953 K, and 1225 K respectively (see Table 3-1). At the higher SPS temperature of 953 K, some of the  $\text{Sr}_2\text{Si}$  was decomposed to  $\text{Sr}_5\text{Si}_3$  (except for in sample B). Balducci et al. also reported on the decomposition of  $\text{Sr}_2\text{Si}$  by following the equilibrium reaction  $3\text{Sr}_2\text{Si}(\text{s}) = \text{Sr}(\text{g}) + \text{Sr}_5\text{Si}_3(\text{s})$  [51]. In Figure 3-2, the  $\text{Sr}_5\text{Si}_3$  peaks appeared in the composite samples C–G. No peak of  $\text{Sr}_5\text{Si}_3$  was observed in samples A or B after SPS. Because of the lower SPS temperature (698 K) for sample A, the SPS pressure (672 MPa) was kept higher to obtain a dense sample. In this study, the composite samples were those that contained the  $\text{Sr}_5\text{Si}_3$  phase that resulted from a higher SPS temperature (953 K), except for sample B. Samples C–G were composite samples having  $\text{Sr}_2\text{Si}$  as a main phase and  $\text{Sr}_5\text{Si}_3$  as a

secondary phase. Sample B was a unique sample because it showed no  $\text{Sr}_5\text{Si}_3$  at a higher SPS temperature. During SPS, the intensity of the  $\text{Sr}_3\text{SiO}$  peaks also increased. Such oxidation is common in the well-studied  $\text{Mg}_2\text{Si}$ , for details see Section 0. In Table 3-1 and Table 3-2, the samples are labeled based on the amount of  $\text{Sr}_5\text{Si}_3$  phase present, which increased going from sample C to H. Dense samples that were almost 100% of the theoretical density were obtained, except for samples A, and G.

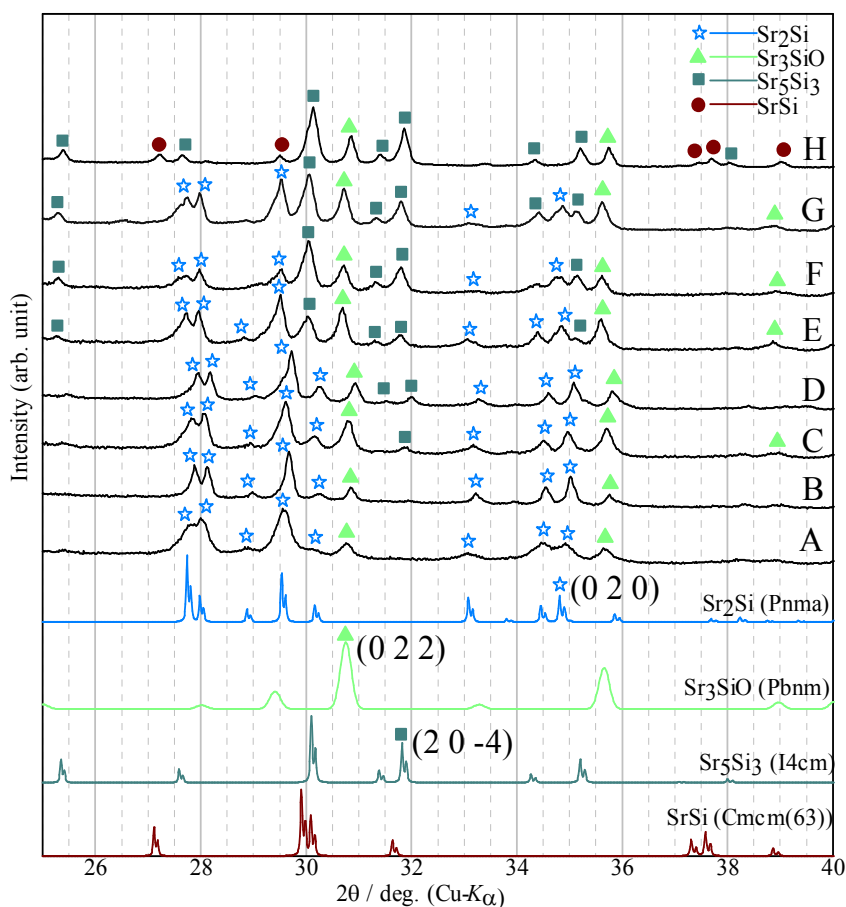


**Figure 3-2 XRD patterns of all samples after SPS**

### 3.2.1.3 After ZEM measurements

The XRD patterns of all samples after ZEM measurements are given in Figure 3-3. All samples were polished and gold sputtered to make contacts for ZEM measurements. Samples A, B and H exhibited  $\text{Sr}_3\text{SiO}$  impurity and sample G minor  $\text{SrSi}$  impurity. In sample A, the peaks at  $2\theta \sim 30^\circ$  (1 0 3), and  $33^\circ$  (0 1 3) were missing. In sample F, the peak at  $2\theta \sim 33^\circ$  (0 1 3) was missing. Possibly owing to the strong orientation texture, which resulted in peak intensities very different from a randomly oriented polycrystalline sample. This was thought to arise from the uniaxial pressure during SPS.

Figure 3-3 shows XRD peaks for the  $\text{Sr}_2\text{Si}$ ,  $\text{Sr}_5\text{Si}_3$ , and  $\text{Sr}_3\text{SiO}$  phases at  $2\theta = 34.81^\circ$  (0 2 0),  $31.83^\circ$  (2 0 -4), and  $30.74^\circ$  (0 2 2), respectively. These did not overlap with the peaks from other phases. To estimate the amount of secondary phases in the samples, the integrated intensity ratios ( $R_{53/21}$ ,  $R_{311/21}$ ) of the above mentioned non-overlapping peaks of the secondary phases were calculated with respect to the main phase peaks, where  $R_{53/21} = I(\text{Sr}_5\text{Si}_3 \text{ (2 0 -4)}) / I(\text{Sr}_2\text{Si (0 2 0)})$  and  $R_{311/21} = I(\text{Sr}_3\text{SiO (0 2 2)}) / I(\text{Sr}_2\text{Si (0 2 0)})$ . The integrated intensity, after subtracting the background intensity and the uncertainty in the integrated intensity of the selected peaks, were obtained by using the PDXL software of the Rigaku company. Figure 3-4 shows the peaks ratios of  $R_{53/21}$ ,  $R_{311/21}$  of secondary phases. For  $\text{Sr}_3\text{SiO}$ , the main peak was considered, while for  $\text{Sr}_2\text{Si}$  and  $\text{Sr}_5\text{Si}_3$ , the main peaks were not considered owing to overlapping. As a result, the value of  $R_{311/21}$  was greater than  $R_{53/21}$  for most of the composite samples. The higher value of  $R_{311/21}$  in Figure 3-4 did not necessarily mean that the amount of  $\text{Sr}_3\text{SiO}$  phase was greater than  $\text{Sr}_2\text{Si}$  and  $\text{Sr}_5\text{Si}_3$  in the composite samples. The  $R_{311/21}$  value of composite samples C-F was almost same,

which indicates these samples have similar amount of oxide. This occurred due to similar SPS conditions of composite samples C-F. Composite sample G showed highest  $R_{311/21}$  and  $R_{53/21}$  values, indicating this sample has highest amounts of  $\text{Sr}_3\text{SiO}$  and  $\text{Sr}_5\text{Si}_3$  phases.

The  $R_{53/21}$  value monotonically increased going from sample C through to G, which indicated that the amount of  $\text{Sr}_5\text{Si}_3$  phase monotonically increased along this series. In sample F and G, the main peak ( $2\theta \sim 30^\circ$ ) of  $\text{Sr}_5\text{Si}_3$  looked larger and equal, respectively, to the second main peak of  $\text{Sr}_2\text{Si}$  ( $2\theta \sim 29.5^\circ$ ), which indicated that the main phase was  $\text{Sr}_5\text{Si}_3$ . However, from the thermal conductivity results and explanation in Section 3.3.1, we concluded that the main phase should be  $\text{Sr}_2\text{Si}$ .

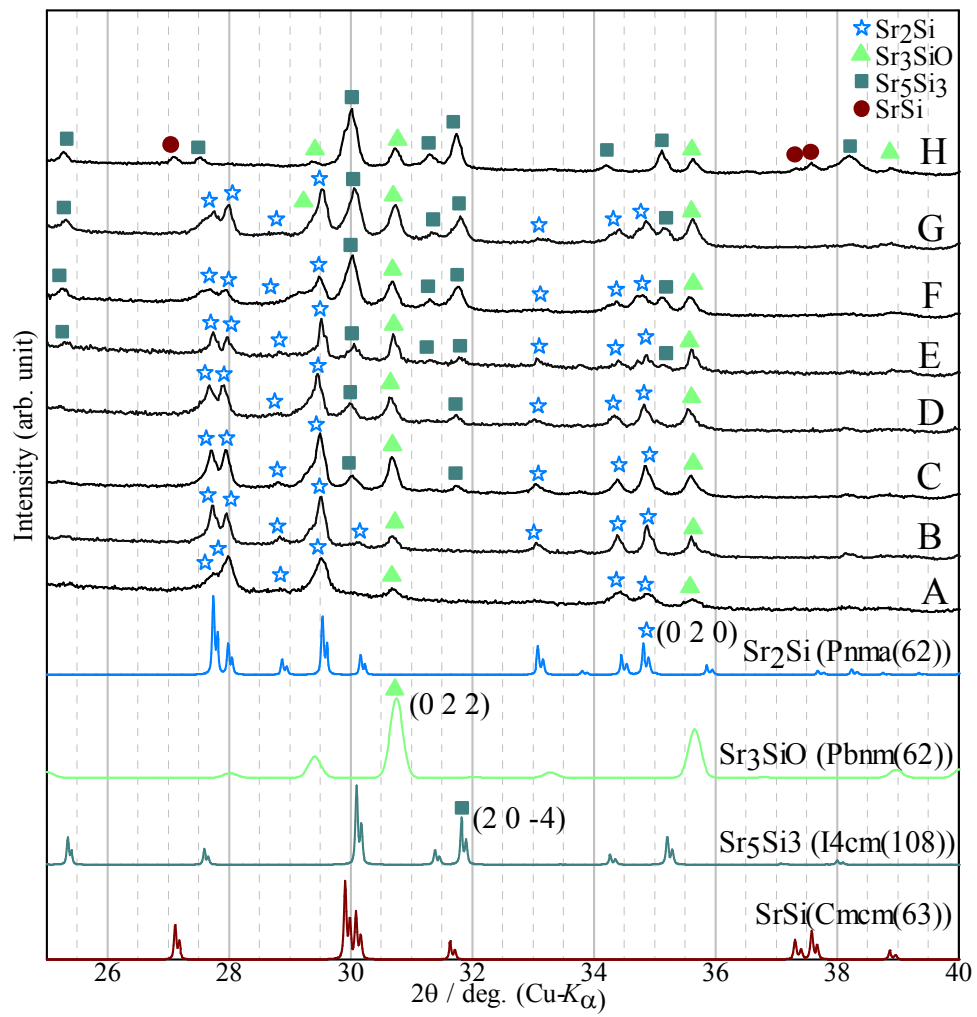


**Figure 3-3 XRD patterns of all samples after ZEM measurements**



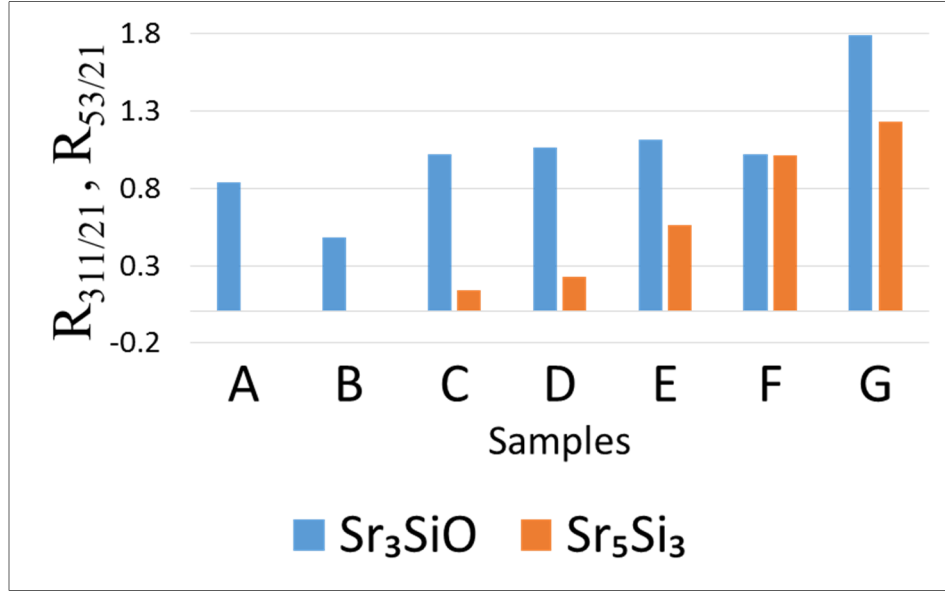


**Figure 3-4 Ratios of XRD peak intensities of secondary phases (Sr<sub>3</sub>SiO, Sr<sub>5</sub>Si<sub>3</sub>) and main phase (Sr<sub>2</sub>Si).  $R_{311/21}$  is the ratio of the Sr<sub>3</sub>SiO (0 2 2) peak to Sr<sub>2</sub>Si (0 2 0) peak.  $R_{53/21}$  is the ratio of the Sr<sub>5</sub>Si<sub>3</sub> (2 0 -4) peak to Sr<sub>2</sub>Si (0 2 0) peak.**

### 3.2.2 Microstructure analysis

Scanning electron microscopy–energy dispersive X-ray spectroscopy (SEM-EDS) of the samples was performed. Here analysis of selected sample is given. The backscattered electron composition image (BEI) of composite sample D showed the presence of three kinds of region: light, dark, and black, as shown in Figure 3-5. Elemental mapping (Figure 3-5 (b), (c), (d)) showed the greatest amounts of Sr and O in the light and dark regions, respectively, suggesting that light regions was main phase of Sr<sub>2</sub>Si. To identify the phases in the dark region, a BEI and secondary electron image (SEI) were obtained at higher magnification, as shown in Figure 3-6. The BEI again showed the presence of three kinds of region: light, dark, and black. Phases in these regions were determined by obtaining the elemental composition by EDS point analysis, as shown in Table 3-3. In Figure

3-6 (a), the light regions corresponded to the  $\text{Sr}_2\text{Si}$  phase and the dark regions corresponded to the  $\text{Sr}_5\text{Si}_3$  and  $\text{Sr}_3\text{SiO}$  phases. The  $\text{Sr}_3\text{SiO}$  phase was observed at the grain boundaries. The black regions corresponded to non-conductive  $\text{SrO}$  particles which appeared on the polished surface of the sample before SEM analysis and were not observed in the XRD results.  $\text{SrO}$  is an insulator and appeared black in the BEI micrograph owing to the accumulation of charge. The exact elemental composition could not be determined by EDS owing to an overlapping of the Sr and Si peaks in the EDS spectrum, which occurred because the X-ray energies of Sr ( $L\alpha$  1.806) and Si ( $K\alpha$  1.740) are very close. The results of the elemental mapping and EDS point analysis were in agreement. The dark region showed a mixture of phases ( $\text{Sr}_3\text{SiO}$ ,  $\text{Sr}_5\text{Si}_3$ , and  $\text{Sr}_2\text{Si}$ ) in the network. It was only possible to identify the  $\text{Sr}_5\text{Si}_3$  phase at higher magnification, thus indicating that the grain size of  $\text{Sr}_5\text{Si}_3$  was quite small relative to that of  $\text{Sr}_2\text{Si}$ .

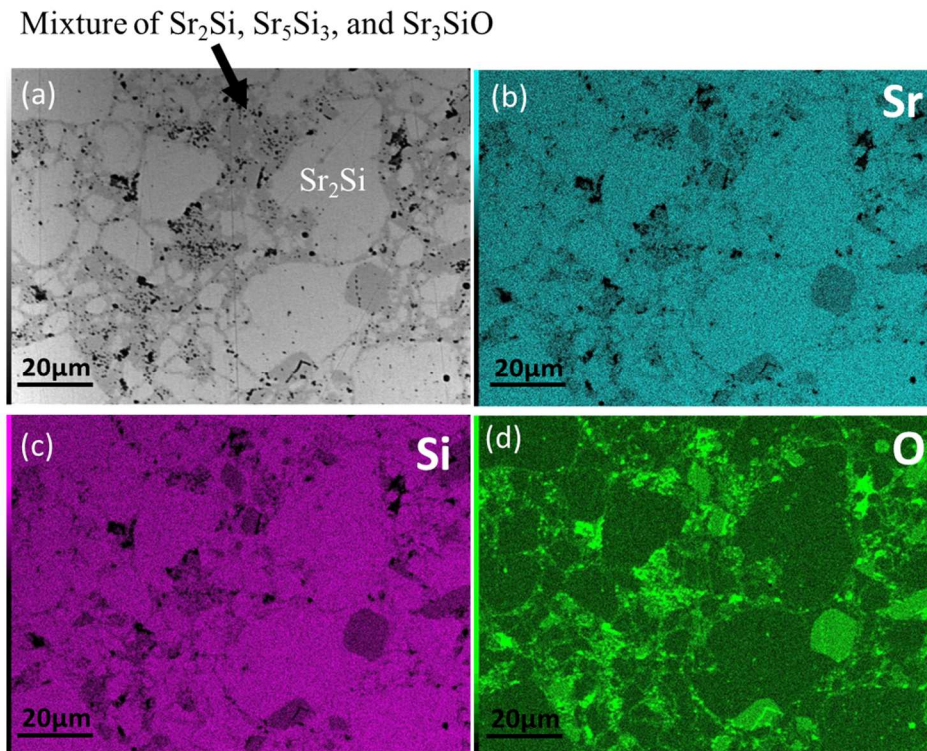


**Figure 3-5 (a) BEI, and (b)–(d) Elemental mapping of composite sample D by SEM-EDS.**

**Table 3-3 Elemental composition of phases determined by EDS point analysis.**

	Atomic percentages				
	Sr <sub>2</sub> Si (U)	Sr <sub>5</sub> Si <sub>3</sub> (V)	Sr <sub>3</sub> SiO (W)	Sr <sub>3</sub> SiO, Grain boundary (X)	SrO (Y)
	Ideal				
	Sr: 66.7	Sr: 62.5	Sr: 60	Sr: 60	Sr: 50
	Si: 33.3	Si: 37.5	Si: 20 O: 20	Si: 20 O: 20	O: 50
	Observed				
Sr	68.0	64.9	63.8	62.8	45.5
Si	27.8	30.8	16.7	23.8	5.1
O	4.21	4.28	19.50	13.5	49.4

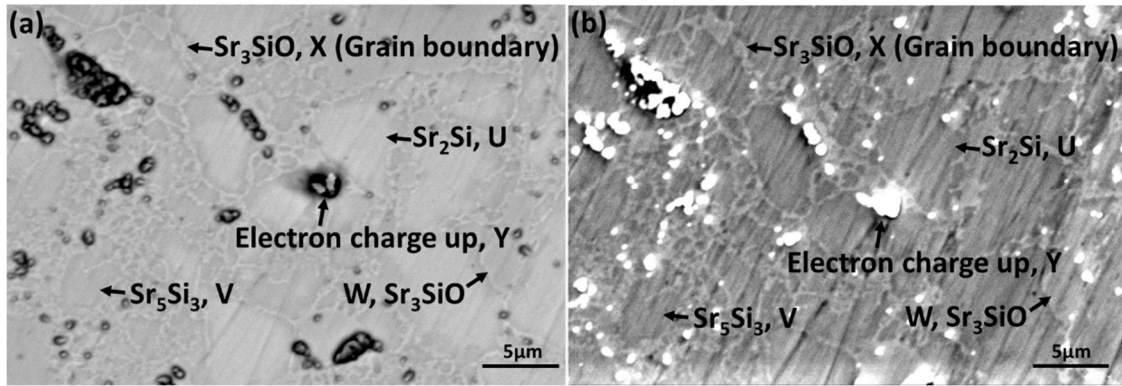


**Figure 3-6 Magnified SEM micrographs of composite sample D. (a) BEI, and (b) SEI.**

### 3.2.3 Thermoelectric properties

The temperature dependence of the  $\rho$ ,  $S$ , and  $P$  of all samples studied are given in Figure 3-7 (a)–(c). The  $\rho$  of composite samples C–G, having  $\text{Sr}_5\text{Si}_3$ , were much lower than those of samples A and B. Sample A showed a higher  $\rho$  than sample B owing to having a lower relative density. The  $\rho$  of samples A–E decreased with an increase in temperature, which was a semiconductor-like behavior except samples F and H. The lowest  $\rho$  was observed from samples F, G (composite) and H (metallic) with a greater amount of the  $\text{Sr}_5\text{Si}_3$  metallic phase, which slightly increased with an increase in temperature (metallic behavior). The  $S$  of the composite samples slightly increased with an increased amount of  $\text{Sr}_5\text{Si}_3$  and with an increase in temperature. The samples having lowest  $\rho$  showed highest  $P$ . ZEM apparatus used in this research could not accurately measure the  $S$  at 300 K, so value of  $S$  and  $P$  are given for temperature above 300 K.

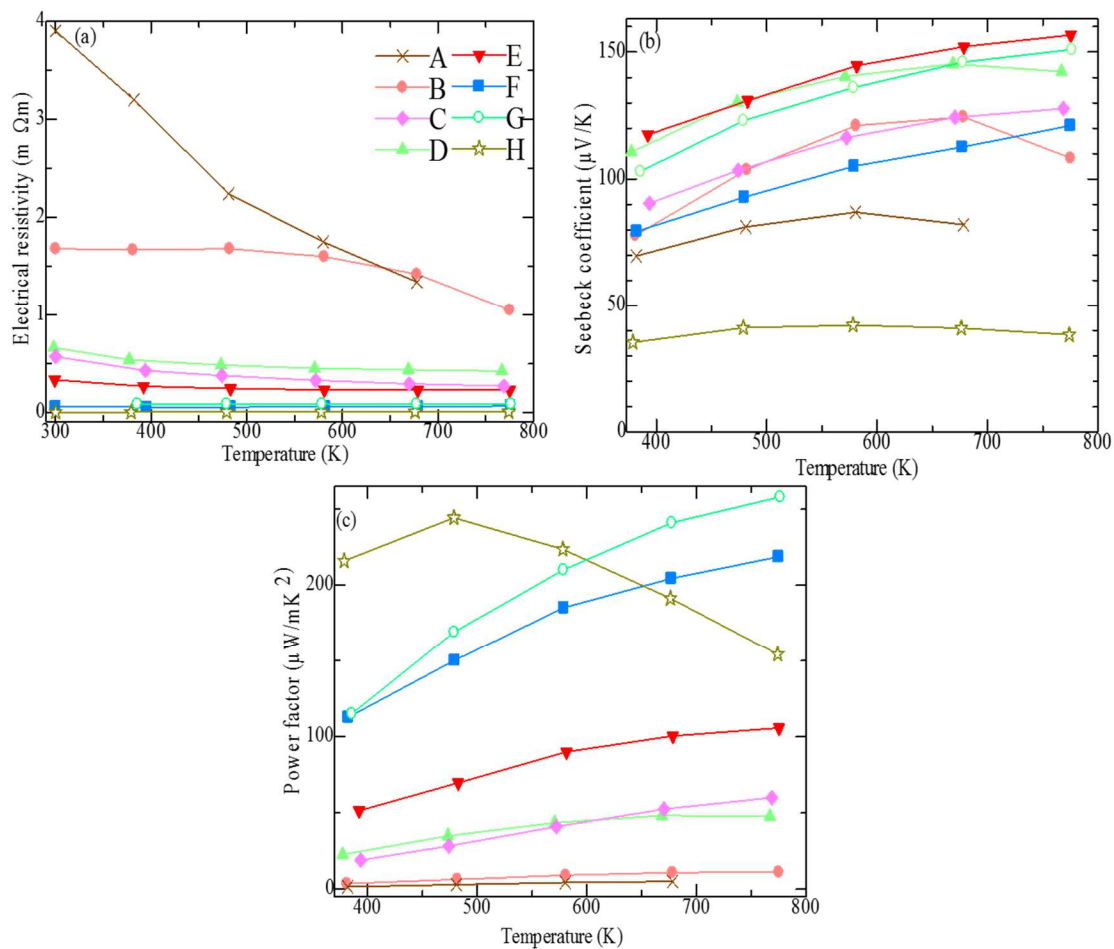


**Figure 3-7 Temperature dependence of (a) electrical resistivity  $\rho$ , (b) Seebeck coefficient  $S$ , and (c) power factor  $P$**

The temperature dependence of  $\kappa$ ,  $\kappa_{el}$ , and  $\kappa_{lat}$  of all samples studied are shown in Figure 3-8 (a)–(c). In all samples except H,  $\kappa$  decreased with an increase in temperature. Sample A, which had no  $\text{Sr}_5\text{Si}_3$  and a low relative density, showed the lowest  $\kappa$ . Metallic sample H showed the highest  $\kappa$ , which first slightly decreased and then increased. The  $\kappa$  of samples B–G lay between that of sample A and that of metallic sample H, though was closer to the former. Although the XRD results after ZEM measurements (Figure 3-3) suggested that the main phase was  $\text{Sr}_5\text{Si}_3$  in sample F and G, but there was no significant difference between  $\kappa$  of all the composite samples. Also, there was

a large difference between  $\kappa$  of composite samples F, and G and metallic sample H. This explains that  $\text{Sr}_2\text{Si}$  was the main phase in samples F and G. Another explanation can be that phonon propagation with grain boundaries increases with increasing amounts  $\text{Sr}_5\text{Si}_3$  in sample F and  $\text{Sr}_5\text{Si}_3$  and  $\text{Sr}_3\text{SiO}$  in samples G, resulting in almost similar  $\kappa$  in all composite samples C-F. Here, we believe in first explanation. As  $\kappa_{el}$  of all samples except metallic sample H was quite low, changing the Lorentz number will not significantly change  $\kappa_{el}$  except for sample H. On the other hand, sample H is metallic and the ideal Lorentz number is usually good for metal. Therefore, constant value of Lorentz number was used for calculating  $\kappa_{el}$  for all the samples using Wiedemann-Franz law:  $\kappa_{el} = L\sigma T$ , where  $L = 2.45 \times 10^{-8} \text{ W}\Omega\text{K}^{-2}$ . Figure 3-8 (b) shows no significant contribution of electronic thermal conductivity in any samples except metallic sample H. In sample H, the room temperature electronic thermal conductivity is nearly half of the total thermal conductivity. There is no significant difference in the  $\kappa_{lat} = \kappa - \kappa_e$  of sample H and samples B–G. Sample A shows the lowest  $\kappa_{lat}$  and  $\kappa$  of all the samples studied. Samples B–G show a monotonic decrease in  $\kappa_{lat}$  and approach  $\kappa_{min}$  (minimum thermal conductivity), which indicates that further decreases in  $\kappa_{lat}$  at higher temperatures can be attained.

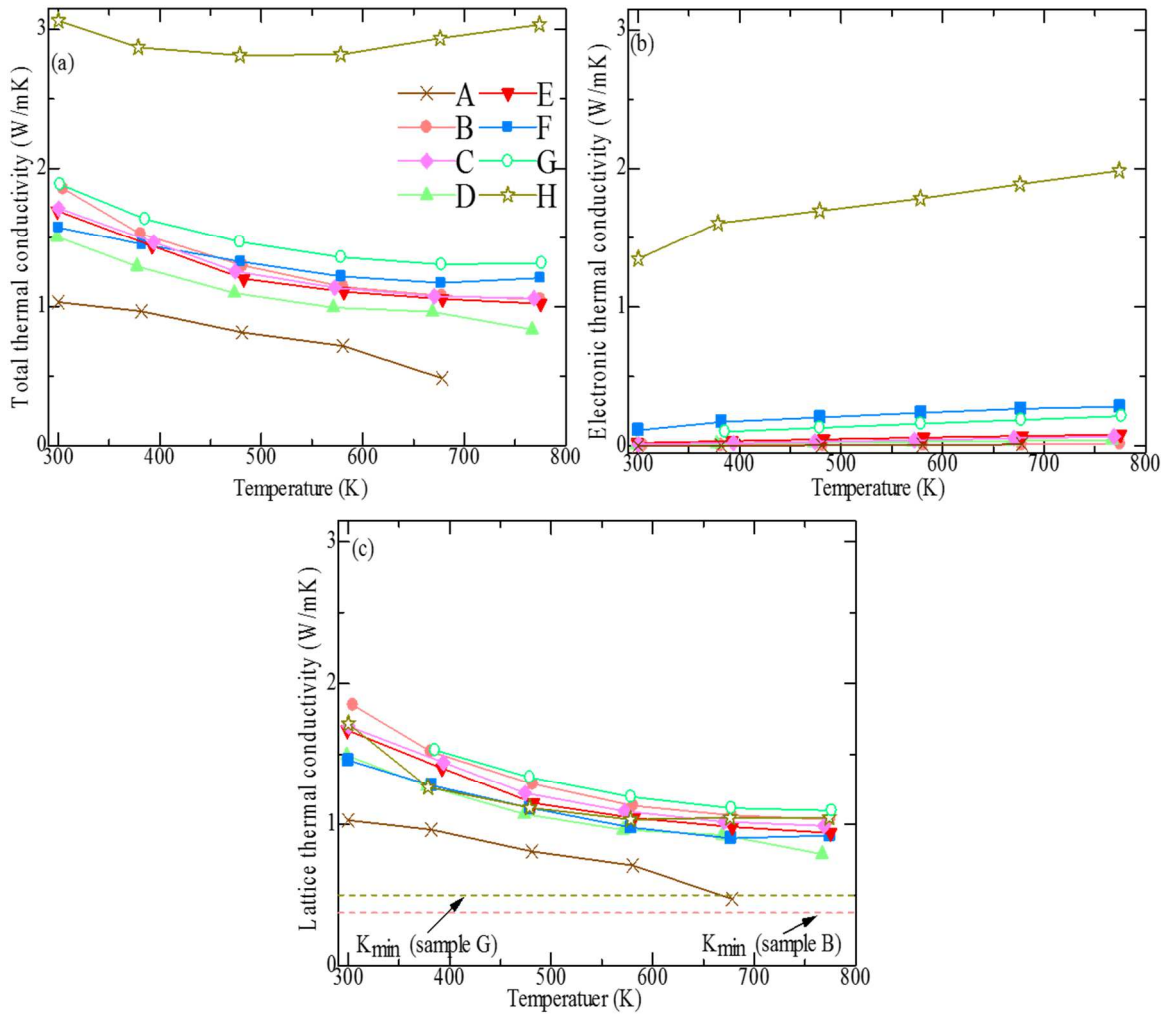


**Figure 3-8 Temperature dependence of (a) total thermal conductivity  $\kappa$ , (b) electronic thermal conductivity  $\kappa_{el}$ , and (c) lattice thermal conductivity  $\kappa_{lat}$ .**

Figure 3-9 shows  $ZT$  for all samples studied. Sample A shows the lowest  $ZT$  because of having the lowest  $P$ , resulting from a higher  $\rho$ . Composite sample G, which has the greatest amount of metallic secondary phase  $Sr_5Si_3$ , shows the highest  $ZT$  of 0.14 at 776 K owing to highest  $P$ . All samples, except H, show a monotonic increase in  $ZT$  because of an increasing  $P$  and decreasing  $\kappa$ , which indicates that further increase in  $ZT$  may be possible at higher temperatures and higher amounts of  $Sr_5Si_3$  phase.

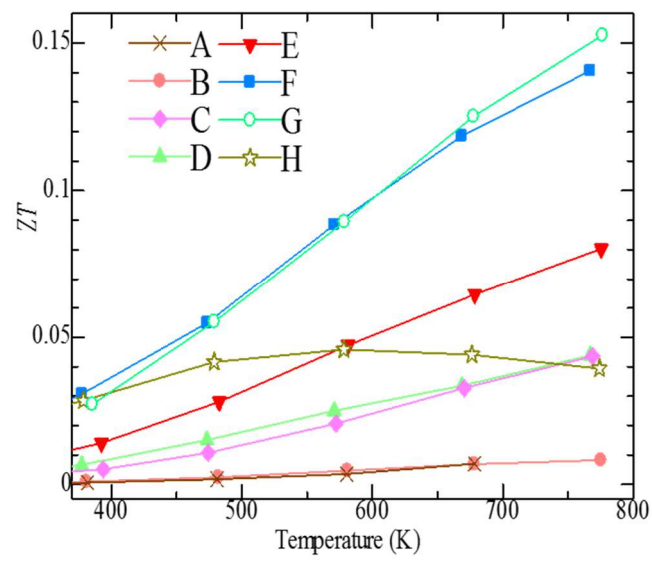


**Figure 3-9 Temperature dependence of dimensionless figure of merit  $ZT$**



### 3.3 Discussion

#### 3.3.1 Effect of composite on thermoelectric properties

To investigate the effect of the composite on the TE properties, data measured at 373 K were plotted against  $R_{311/21}$  and  $R_{53/21}$  values for samples B–G, shown in Figure 3-10, and Figure 3-11, respectively. The  $R_{311/21}$  and  $R_{53/21}$  values are obtained from Figure 3-4. For details of  $R_{311/21}$  and  $R_{53/21}$ , see Section 3.2.1.3.  $R_{311/21}$  values are similar for composite samples C–F, which meant the amounts of the oxide phase were similar in these samples owing to the same SPS conditions. The  $R_{311/21}$  value of composite sample G is greater than sample F but the  $\rho$  difference is not significant. No clear relationship between the  $R_{311/21}$  values and TE properties was found. However,  $\rho$ ,  $P$ , and  $ZT$  showed a strong relationship to the  $R_{53/21}$  values, while  $S$  and  $\kappa$  did not.  $\rho$  decreased, while  $P$  and  $ZT$  almost linearly increased with  $R_{53/21}$ , that is, the amount of the  $\text{Sr}_5\text{Si}_3$  phase present.

The reason for  $\rho$  decreasing with an increasing  $R_{53/21}$  was considered to arise from the composite effect that was explained in the Section 1.5. The presence of the greater electrical conductivity metallic  $\text{Sr}_5\text{Si}_3$  phase at the grain boundaries contributed to the reduction in  $\rho$  for the composite samples C–G. The sign of  $S$  was positive for all samples, thus indicating that the majority of carriers were holes.  $S$  often decreases with a decrease in  $\rho$  in the composite effect, as well as through the carrier control effect, see Section 1.6. In the present case, first  $S$  increased with the increasing amount of  $\text{Sr}_5\text{Si}_3$  phase, and then decreased for the sample F, G having the greatest amount of  $\text{Sr}_5\text{Si}_3$  phase, however,  $\rho$  decreased for all samples. This may possibly be a result of the carrier control effect, that is, the hole carrier density of the  $\text{Sr}_2\text{Si}$  main phase decreased (Section 1.7) and  $S$  increased with an increase in  $R_{53/21}$ . A similar behavior has been reported for the  $\text{Ca}_3\text{Co}_4\text{O}_9$  [39] and  $\text{YB}_{22}\text{C}_2\text{N}$  [40] systems possessing an increased amount of the higher conductive ( $\text{Bi}_2\text{O}_3$  and  $\text{VB}_2$ ) phases, respectively, explained in Section 1.7. In the present case,

electron doping, that is, decreasing the hole carrier density, can be introduced by increasing the Sr concentration, that is, decreasing the number of Sr vacancies, in the  $\text{Sr}_2\text{Si}$  phase. However, this seems not to be realized with an increasing amount of Sr-poor  $\text{Sr}_5\text{Si}_3$  phase. Another possible mechanism of increasing  $S$  is the energy filtering effect (Section 1.5.2.2), that is, the scattering rate of the hole carrier at the boundary between  $\text{Sr}_2\text{Si}$  and  $\text{Sr}_5\text{Si}_3$  depends on the energy of the carrier [37]. Therefore, to clarify the mechanism of increased  $S$  with decreased  $\rho$ , further investigation is needed. The highest  $S$  value of  $119 \mu\text{V/K}$  at  $373 \text{ K}$  was shown by composite sample E, and this increased to  $157 \mu\text{V/K}$  at  $773 \text{ K}$ .  $\kappa$  of composite samples C–F was closer to samples A and B having no  $\text{Sr}_5\text{Si}_3$ , which also indicated that the main phase in the composite samples was  $\text{Sr}_2\text{Si}$ . There was a slight difference in  $\kappa$  of composite samples C–G, which indicated that there was a slight difference in the amount of  $\text{Sr}_5\text{Si}_3$  in these samples. As a result, composite samples may have a similar concentration of grain boundaries and phonon scattering. All composite samples showed an increase in  $P$  and  $ZT$  with  $R_{53/21}$  except sample G. In case of sample G,  $P$  saturated and  $ZT$  decreased slightly (Figure 3-11 (e)) but at high temperature  $P$  and  $ZT$  were highest (Figure 3-9), which indicates further increase in  $P$  and  $ZT$  is possible with  $R_{53/21}$  at higher temperatures.

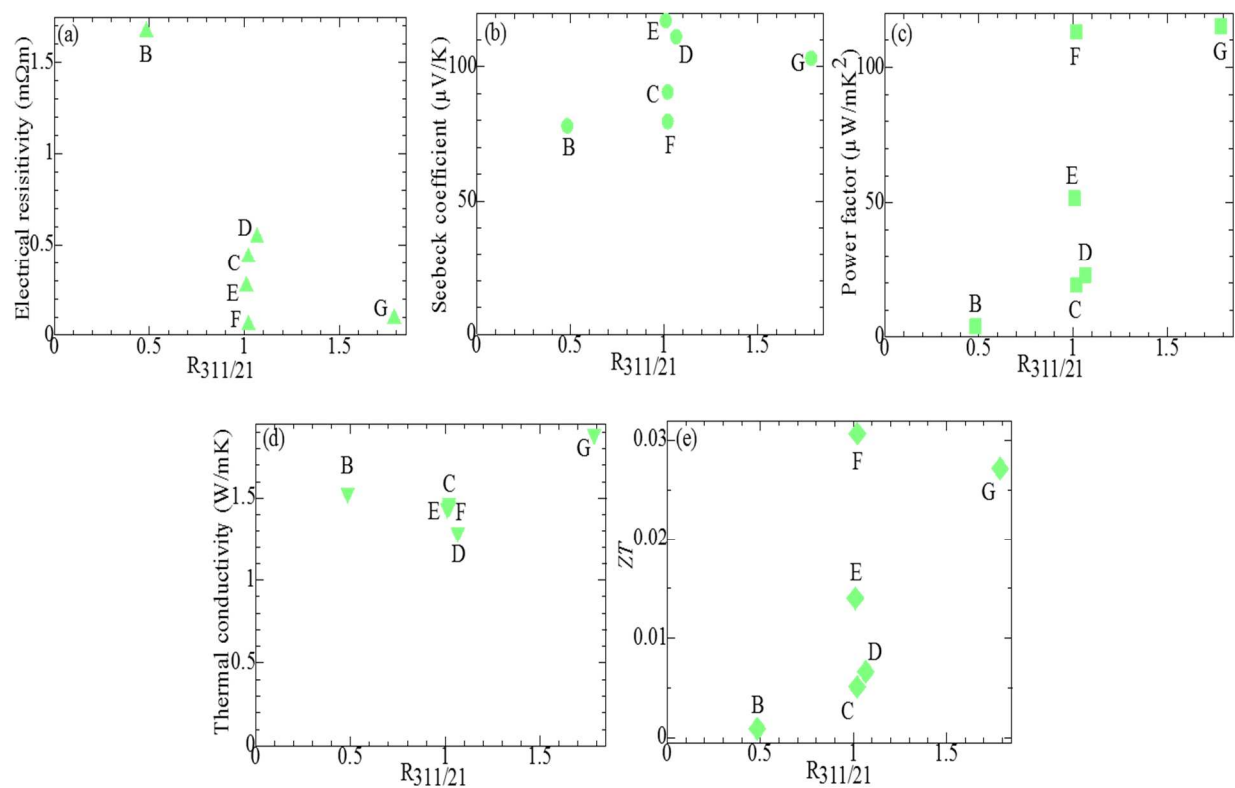


**Figure 3-10 (a)–(e) Dependence of transport properties at 373 K on  $R_{311/21}$ , i.e., the amount of  $\text{Sr}_3\text{SiO}$  phase present in the system.**

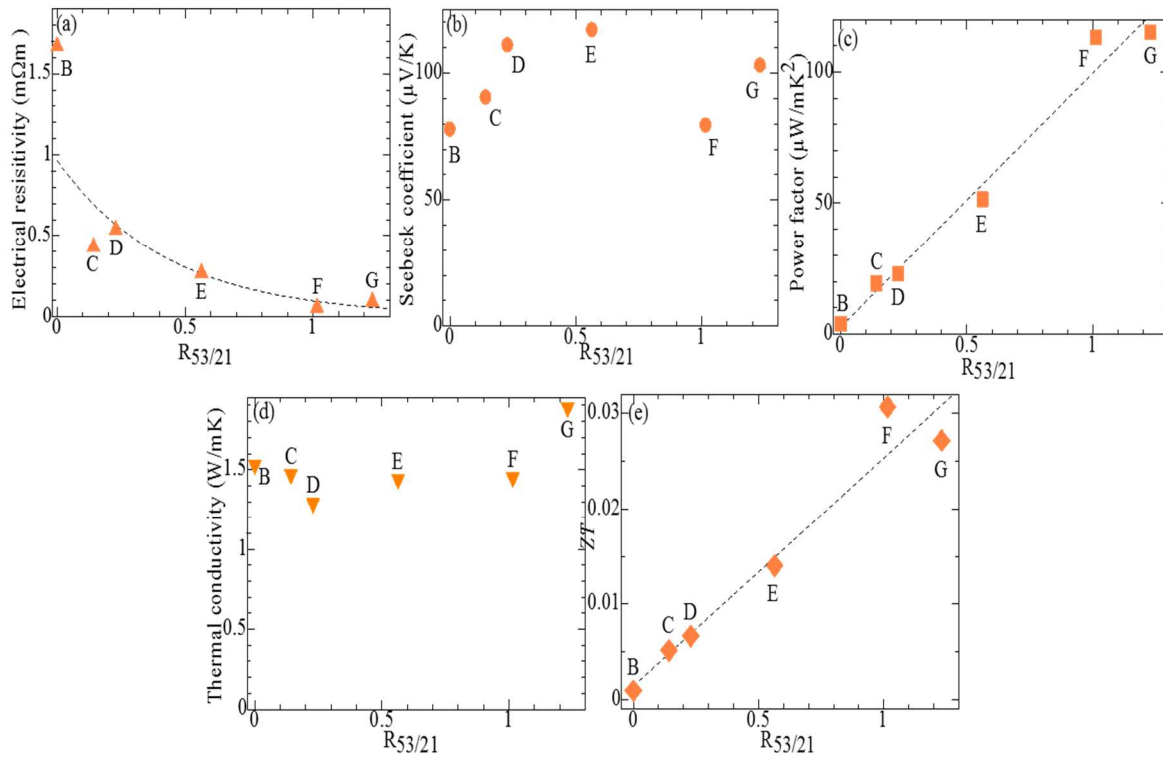


**Figure 3-11 (a)–(e) Dependence of transport properties at 373 K on  $R_{53/21}$ , i.e., the amount of  $Sr_5Si_3$  phase present in the system.**

Although the sample preparation was carefully carried out using a glovebox, all samples A–H included the oxide  $Sr_3SiO$  phase. This situation was similar to that witnessed for  $Mg_2Si$  that was reported previously, explained in Section 0.  $MgO$  is known for the oxidation of  $Mg_2Si$  after synthesis and sintering, and traces of  $MgO$  were found even in the high  $ZT$  samples [52–54].

The bandgap of orthorhombic  $Sr_2Si$  has been reported to be 0.40 eV [42,43] and 0.29 eV [1]. In the measured high-temperature range, the resistivity characteristics would be in or near the intrinsic region for  $Sr_2Si$  with a narrow bandgap of approximately 0.3 eV. As shown in Figure 3-12, the temperature dependence of  $\rho$  revealed that the activation energy was approximately 0.13 eV, which was close to half of the calculated electronic bandgap mentioned above. The similar

orthorhombic crystal structure of  $\text{Ca}_2\text{Si}$  also showed the activation energy of the resistivity to be approximately 0.13 eV, which was also close to half of its calculated bandgap [49].

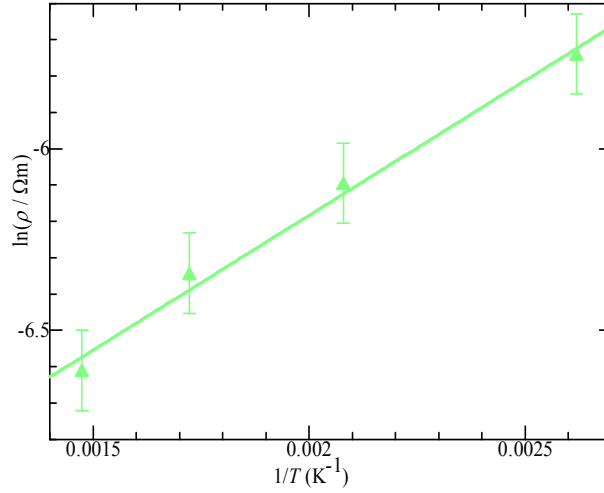


**Figure 3-12 Arrhenius plot of electrical resistivity versus inverse temperature. Error in TE properties was calculated by considering uncertainty in sample dimensions and instruments**

### 3.3.2 Origin of low lattice thermal conductivity

A low lattice thermal conductivity,  $\kappa_{\text{lat}}$ , is necessary to obtain a high  $ZT$ . Decreasing  $\kappa_{\text{lat}}$ , as determined by phonon propagation, has been one of the main motivations behind TE research in recent decades. Composite samples C–G and non-composite samples B and H (metallic), have very similar  $\kappa_{\text{lat}}$ . To understand the origin of the low lattice thermal conductivity in the samples studied herein, their physical properties were measured and estimated. Longitudinal ( $v_l$ ) and transverse ( $v_s$ ) sound velocities were measured at room temperature in air. The average sound velocity ( $v_{\text{ave}}$ ) and the Debye temperature ( $\theta_D$ ) were calculated by the following equations:

$$v_{\text{ave}} = [1/3(1/v_l^3 + 2/v_s^3)]^{-1/3} \quad \text{Eq. 3-1}$$

$$\theta_D = (h/k_B)(3N/4\pi V)^{1/3} v_{\text{ave}} \quad \text{Eq. 3-2}$$

where  $h$  is the Planck's constant,  $K_B$  is the Boltzmann constant,  $N$  is the number of atoms in the unit cell, and  $V$  is the unit cell volume. The physical properties were only calculated for samples B and H having  $\text{Sr}_2\text{Si}$  and  $\text{Sr}_5\text{Si}_3$  as the main phase, respectively. Sample A having  $\text{Sr}_2\text{Si}$  as a main phase, was not considered for investigating low lattice thermal conductivity due to having lower relative density. The sound velocities for  $\text{BaSi}_2$ ,  $\text{LaSi}$ , and  $\text{SrSi}_2$  were taken from Ref. [13].

**Table 3-4 Thermophysical properties of strontium silicide samples together with the literature data.**

	$v_l$ (km/s)	$v_s$ (km/s)	$v_{ave}$ (km/s)	$\theta_D$ (K)	$M\delta(\theta_D)^3 / N^{2/3} T$	$\kappa_{lat}$	Ref.
A	3.2	2.1	2.3	-	-	-	This work
B	4.0	2.4	2.6	240	2.0E-04	1.8	This work
C	4.1	2.9	3.1	-	-	-	This work
D	4.3	2.5	2.7	-	-	-	This work
E	4.2	2.5	2.7	-	-	-	This work
H	4.6	2.7	3.0	290	1.3E-04	1.7	This work
BaSi <sub>2</sub>	4.170	2.470	2.736	265	1.48E-04	1.38	[13]
LaSi	3.690	2.240	2.475	251	3.22E-04	3.06	[13]
SrSi <sub>2</sub>	5.800	3.260	3.627	378	4.71E-04	4.26	[13]
Mg <sub>2</sub> Si	-	-	-	-	14.3E-04	10.9	[13]

As discussed in Section 1.2.8.1, theoretical lattice thermal conductivity,  $\kappa_{\text{lat}}'$ , is proportional to  $M\delta(\theta_D)^3 / N^{2/3}T$  (Eq. 1-5).  $\kappa_{\text{lat}}'$  was calculated at 300 K for the samples B, H, BaSi<sub>2</sub>, LaSi, and SrSi<sub>2</sub>. Figure 3-13 shows the experimental lattice thermal conductivity,  $\kappa_{\text{lat}}$ , at 300 K as a function of  $M\delta(\theta_D)^3 / N^{2/3}T$  ( $T = 300$  K), together with the literature data. The present results exhibit that a decreased value for  $M\delta(\theta_D)^3 / N^{2/3}T$  leads to a decrease in  $\kappa_{\text{lat}}$  at 300 K. This indicated that  $\kappa_{\text{lat}}$  is proportional to  $\kappa_{\text{lat}}'$ , which obeys Eq 1-5. This means that the effect of oxide is not significant because all samples contained minor amounts of oxide (Sr<sub>3</sub>SiO) impurity. Values of  $v_{\text{ave}}$ ,  $\theta_D$ ,  $M\delta(\theta_D)^3 / N^{2/3}T$  and  $\kappa_{\text{lat}}$  (at 300 K) are summarized in Table 3-4. However, Peng et al. reported a significant influence of MgO in the lattice thermal conductivity of Mg<sub>2</sub>Si [55]. Parameter  $M\delta(\theta_D)^3 / N^{2/3}T$  for Mg<sub>2</sub>Si is taken from Ref. [13]. Eq. 1-5 can be expressed using independent physical properties as:

$$\kappa_{\text{lat}}' \propto K^{3/2} / M^{1/2} \delta^2 N^{2/3} T \quad \text{Eq. 3-3}$$

where  $K$  is the average atomic force constant of the constituent elements. From Eq. 3-3, the origin of a low  $\kappa_{\text{lat}}$  may be considered to be from weak atomic bonds, higher atomic mass, large atomic volume, and a large number of atoms in the unit cell.

The minimum thermal conductivity,  $\kappa_{\text{min}}$ , was calculated by Eq. 3-4 [56] and was found to be 0.38 W/mK and 0.5 W/mK for samples B and G, respectively, as shown in Figure 3-8 (c).

$$\kappa_{\text{min}} \sim 1.2 k_B v_{\text{ave}} / \delta^2 \quad \text{Eq. 3-4}$$



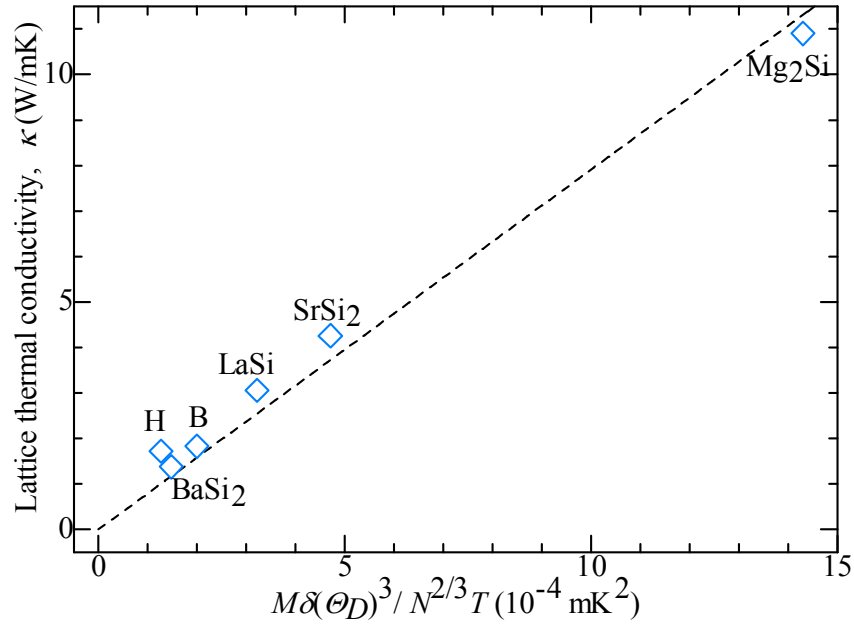


**Figure 3-13 Relationship between  $(M\delta(\theta_D)^3 / N^{2/3} T, T=300 \text{ K})$  and  $\kappa_{\text{lat}}$  for samples B ( $\text{Sr}_2\text{Si}$ ) and H ( $\text{Sr}_5\text{Si}_3$ ), together with literature data for  $\text{BaSi}_2$ ,  $\text{SrSi}_2$ ,  $\text{LaSi}$ , and  $\text{Mg}_2\text{Si}$  taken from Ref. [13].**

### 3.3.3 Lowest thermal conductivity silicide

The low  $\kappa_{\text{lat}} = 1.8 \text{ W/mK}$  of  $\text{Sr}_2\text{Si}$  (sample B) at room temperature was comparable with those of typical TE materials, such as  $\text{Bi}_2\text{Te}_3$ :  $\kappa_{\text{lat}} = 0.68\text{--}0.90 \text{ W/mK}$ , and  $ZT = 0.82\text{--}1.05$  at 300–400 K [57]. Room temperature  $\kappa_{\text{lat}}$  values of  $\text{Ca}_2\text{Si}$ ,  $\text{SrSi}_2$ ,  $\text{Si}_{80}\text{Ge}_{20}$ , and  $\text{Mg}_2\text{Si}_{1-x}\text{Bi}_x$  are 2.31 W/mK [49], 6.5 W/mK [58], 4 W/mK [59], and 6.68 W/mK [60], respectively. The low  $\kappa_{\text{lat}}$  for  $\text{Sr}_2\text{Si}$  is one of the lowest among the known silicides, but is still higher than the minimum lattice thermal conductivity value of 0.38 W/mK, as calculated by Eq. 3-4, which was the approach used by Cahill

[61]. This seems to leave room for a further reduction to be obtainable, which justifies even higher  $ZT$  values.

### 3.4 Summary

1.  $\text{Sr}_2\text{Si}$  and  $\text{Sr}_5\text{Si}_3$  samples were obtained by reacting Sr and  $\text{SrSi}_2$  with minor amounts of  $\text{Sr}_3\text{SiO}$  impurity.
2. Composites of  $\text{Sr}_2\text{Si}$  and  $\text{Sr}_5\text{Si}_3$  were obtained by the SPS process.
3. Microstructural analysis demonstrated that in composite samples,  $\text{Sr}_2\text{Si}$  grains were surrounded by a mixture of smaller grains of  $\text{Sr}_2\text{Si}$ ,  $\text{Sr}_5\text{Si}_3$ , and  $\text{Sr}_3\text{SiO}$ .
4. The reduction in the electrical resistivity was remarkable in the presence of the metallic  $\text{Sr}_5\text{Si}_3$  phase, and was further decreased with an increased amount of  $\text{Sr}_5\text{Si}_3$ .
5. However, the positive Seebeck coefficient first increased with the increasing amount of  $\text{Sr}_5\text{Si}_3$  phase, and then decreased for the sample having the greatest amount of  $\text{Sr}_5\text{Si}_3$  phase, which could be explained by electron doping (decrease of hole carrier concentration) or energy-filtering of carriers.
6. The thermal conductivities (lattice thermal conductivity was dominant) were largely unaffected by the presence of either the metallic  $\text{Sr}_5\text{Si}_3$  or semiconducting  $\text{Sr}_3\text{SiO}$  phases.
7. As a result, the power factor and  $ZT$  increased almost linearly with an increased amount of  $\text{Sr}_5\text{Si}_3$ , both by composite and carrier control effects.
8. Maximum  $ZT$  was achieved in the composite samples that had the greatest amount of  $\text{Sr}_5\text{Si}_3$  phase present.

9. The electrical resistivity significantly decreased and Seebeck coefficient slightly increased, which was quite different from the conventional composite or carrier control effects. This suggested that there is a significant potential for enhancing  $ZT$  in  $\text{Sr}_2\text{Si}$ - $\text{Sr}_5\text{Si}_3$  composites.
10. The lattice thermal conductivity of the  $\text{Sr}_2\text{Si}$  phase was among the lowest of known, typical silicides and was consistent with the formula proposed by Slack.
11. Possible reasons for the lower lattice thermal conductivity of  $\text{Sr}_2\text{Si}$  are weak atomic bonds, heavy atomic mass, large atomic volume, and a large number of atoms in the unit cell.
12. The  $ZT$  values of composites of  $\text{Sr}_2\text{Si}$  and  $\text{Sr}_5\text{Si}_3$  are expected to increase at higher temperatures and when a greater amount of the  $\text{Sr}_5\text{Si}_3$  phase is present.

## **Publications**

F. Mudasar, Y. Katsura, K. Kitahara, K. Kimura, Enhanced thermoelectric figure of merit by composite effects and low thermal conductivity in distronium silicide ( $\text{Sr}_2\text{Si}$ ), Journal of Alloys and Compounds (2019), <https://doi.org/10.1016/j.jallcom.2018.12.037>.

## **Conferences**

1. The 6th GPSS-GLI International Symposium “Framing to Action: Bringing Sustainability Thinking into Practice”, University of Tokyo, Kashiwa Campus (March 2018)
2. Symposium on Bridging Nature and Technology, University of Tokyo, Hongo Campus (December 2017)
3. International Conference on Thermoelectrics-2017, Los Angeles, California (August 2017).

## References

- [1] S. Brutti, D. Nguyen-Manh, D. G. Pettifor, Lattice stability of intermediate phases of the Sr–Si system, *Journal of Alloys and Compounds*. 457 (2008) 29–35. doi:10.1016/j.jallcom.2007.03.023.
- [2] Key World Energy Statistics, <https://www.iea.org/statistics/kwes/> (accessed November 25, 2018).
- [3] O. Edenhofer, Intergovernmental Panel on Climate Change, Working Group 3, Renewable energy sources and climate change mitigation: summary for policymakers and technical summary: special report of the intergovernmental panel on climate change, Cambridge University Press, New York, 2011.
- [4] M. Höök, J. Li, K. Johansson, S. Snowden, Growth Rates of Global Energy Systems and Future Outlooks, *Natural Resources Research*. 21 (2012) 23–41. doi:10.1007/s11053-011-9162-0.
- [5] C. Forman, I. K. Muritala, R. Pardemann, B. Meyer, Estimating the global waste heat potential, *Renewable and Sustainable Energy Reviews*. 57 (2016) 1568–1579. doi:10.1016/j.rser.2015.12.192.
- [6] L. E. Bell, Cooling, Heating, Generating Power, and Recovering Waste Heat with Thermoelectric Systems, *Science*. 321 (2008) 1457–1461. doi:10.1126/science.1158899.
- [7] M. Rull-Bravo, A. Moure, J. F. Fernández, M. Martín-González, Skutterudites as thermoelectric materials: revisited, *RSC Advances*. 5 (2015) 41653–41667. doi:10.1039/C5RA03942H.
- [8] C. Gayner, K. K. Kar, Recent advances in thermoelectric materials, *Progress in Materials Science*. 83 (2016) 330–382. doi:10.1016/j.pmatsci.2016.07.002.
- [9] J. P. Fleurial, Thermoelectric power generation materials: Technology and application opportunities, *Journal of Materials*. 61 (2009) 79–85. doi:10.1007/s11837-009-0057-z.
- [10] J. P. Heremans, V. Jovovic, E. S. Toberer, A. Saramat, K. Kurosaki, A. Charoenphakdee, S. Yamanaka, G. J. Snyder, Enhancement of Thermoelectric Efficiency in PbTe by Distortion of the Electronic Density of States, *Science*. 321 (2008) 554–557. doi:10.1126/science.1159725.
- [11] G. J. Snyder, E. S. Toberer, Complex thermoelectric materials, *Nature Materials*. 7 (2008) 105–114. doi:10.1038/nmat2090.
- [12] R. E. Hummel, *Electronic properties of materials*. 2001, 3rd ed., New York, Springer.
- [13] K. Hashimoto, K. Kurosaki, Y. Imamura, H. Muta, S. Yamanaka, Thermoelectric properties of BaSi<sub>2</sub>, SrSi<sub>2</sub>, and LaSi, *Journal of Applied Physics*. 102 (2007) 063703. doi:10.1063/1.2778747.

- [14] G. A. Slack, Solid State Physics: Advances in Research and Applications, edited by H. Ehrenreich, F. Seitz, and D. Turnbull (Academic, New York, 1979), Vol. 34.
- [15] D. K. Aswal, R. Basu, A. Singh, Key issues in development of thermoelectric power generators: High figure-of-merit materials and their highly conducting interfaces with metallic interconnects, *Energy Conversion and Management*. 114 (2016) 50–67. doi:10.1016/j.enconman.2016.01.065.
- [16] A. Nozariasbmarz, A. Agarwal, Z. A. Coutant, M. J. Hall, J. Liu, R. Liu, A. Malhotra, P. Norouzzadeh, M. C. Öztürk, V. P. Ramesh, Y. Sargolzaeiaval, F. Suarez, D. Vashaee, Thermoelectric silicides: A review, *Japanese Journal of Applied Physics*. 56 (2017) 05DA04. doi:10.7567/JJAP.56.05DA04.
- [17] M. I. Fedorov, G. N. Isachenko, Silicides: Materials for thermoelectric energy conversion, *Japanese Journal of Applied Physics*. 54 (2015) 07JA05. doi:10.7567/JJAP.54.07JA05.
- [18] S. LeBlanc, Thermoelectric generators: Linking material properties and systems engineering for waste heat recovery applications, *Sustainable Materials and Technologies*. 1–2 (2014) 26–35. doi:10.1016/j.susmat.2014.11.002.
- [19] R. Morris, Semiconducting properties of  $\text{Mg}_2\text{Si}$  single crystals, *Retrospective Theses and Dissertations*. (1957). doi:<https://doi.org/10.31274/rtd-180813-3350>.
- [20] C. Austin, Environmental-friendly thermoelectric materials, Honours Thesis, The University of Queensland, 2016. <https://doi.org/10.14264/uql.2017.231>.
- [21] H. Udono, H. Tajima, M. Uchikoshi, M. Itakura, Crystal growth and characterization of  $\text{Mg}_2\text{Si}$  for IR-detectors and thermoelectric applications, *Japanese Journal of Applied Physics*. 54 (2015) 07JB06. doi:10.7567/JJAP.54.07JB06.
- [22] W. Liu, Q. Zhang, K. Yin, H. Chi, X. Zhou, X. Tang, C. Uher, High figure of merit and thermoelectric properties of Bi-doped  $\text{Mg}_2\text{Si}_{0.4}\text{Sn}_{0.6}$  solid solutions, *Journal of Solid State Chemistry*. 203 (2013) 333–339. doi:10.1016/j.jssc.2013.04.041.
- [23] Y. Imamura, H. Muta, K. Kurosaki, S. Yamanaka, Thermoelectric properties of calcium silicides, 25th International Conference on Thermoelectrics, (2006) 535–538. doi:10.1109/ICT.2006.331351.
- [24] M. J. Yang, L. M. Zhang, L. Q. Han, Q. Shen, C. B. Wang, Simple fabrication of  $\text{Mg}_2\text{Si}$  thermoelectric generator by spark plasma sintering, *Indian Journal of Engineering and Material Science* (2009) 4.
- [25] Y. Mito, A. Ogino, S. Konno, H. Udono, Influence of Humidity, Volume Density, and MgO Impurity on  $\text{Mg}_2\text{Si}$  Thermoelectric-Leg, *Journal of Electronic Materials*. 46 (2017) 3103–3108. doi:10.1007/s11664-016-5182-1.
- [26] S. Fiameni, S. Battiston, S. Boldrini, A. Famengo, F. Agresti, S. Barison, M. Fabrizio, Synthesis and characterization of Bi-doped  $\text{Mg}_2\text{Si}$  thermoelectric materials, *Journal of Solid State Chemistry*. 193 (2012) 142–146. doi:10.1016/j.jssc.2012.05.004.

- [27] Y. Ma, R. Heijl, A. E. C. Palmqvist, Composite thermoelectric materials with embedded nanoparticles, *Journal of Material Science*. 48 (2013) 2767–2778. doi:10.1007/s10853-012-6976-z.
- [28] R. Venkatasubramanian, E. Siivola, T. Colpitts, B. O’Quinn, Thin-film thermoelectric devices with high room-temperature figures of merit, *Nature*. 413 (2001) 597–602. doi:10.1038/35098012.
- [29] D. M. Rowe, V. S. Shukla, N. Savvides, Phonon scattering at grain boundaries in heavily doped fine-grained silicon–germanium alloys, *Nature*. 290 (1981) 765–766. doi:10.1038/290765a0.
- [30] W. Kim, J. Zide, A. Gossard, D. Klenov, S. Stemmer, A. Shakouri, A. Majumdar, Thermal Conductivity Reduction and Thermoelectric Figure of Merit Increase by Embedding Nanoparticles in Crystalline Semiconductors, *Physical Review Letters*. 96 (2006) 045901. doi:10.1103/PhysRevLett.96.045901.
- [31] C. M. Bhandari, Minimizing the thermal conductivity, *CRC Handbook of Thermoelectrics*, CRC Press LLC, Boca Raton, Edited by D. M. Rowe, (1995) p 55.
- [32] R. Prasher, Thermal Transport Due to Phonons in Random Nano-particulate Media in the Multiple and Dependent (Correlated) Elastic Scattering Regime, *Journal of Heat Transfer*. 128 (2006) 627–637. doi:10.1115/1.2194036.
- [33] N. Mingo, D. Hauser, N. P. Kobayashi, M. Plissonnier, A. Shakouri, “Nanoparticle-in-Alloy” Approach to Efficient Thermoelectrics: Silicides in SiGe, *Nano Letters*. 9 (2009) 711–715. doi:10.1021/nl8031982.
- [34] W. Kim, A. Majumdar, Phonon scattering cross section of polydispersed spherical nanoparticles, *Journal of Applied Physics*. 99 (2006) 084306. doi:10.1063/1.2188251.
- [35] J. M. O. Zide, D. Vashaee, Z. X. Bian, G. Zeng, J. E. Bowers, A. Shakouri, A. C. Gossard, Demonstration of electron filtering to increase the Seebeck coefficient in  $\text{In}_{0.53}\text{Ga}_{0.47}\text{As}/\text{In}_{0.53}\text{Ga}_{0.28}\text{Al}_{0.19}\text{As}$  superlattices, *Physical Review B*. 74 (2006) 205335. doi:10.1103/PhysRevB.74.205335.
- [36] J. P. Heremans, C. M. Thrush, D. T. Morelli, Thermopower enhancement in PbTe with Pb precipitates, *Journal of Applied Physics*. 98 (2005) 063703. doi:10.1063/1.2037209.
- [37] S. V. Faleev, F. Léonard, Theory of enhancement of thermoelectric properties of materials with nano-inclusions, *Phys. Rev. B*. 77 (2008) 214304. doi:10.1103/PhysRevB.77.214304.
- [38] D. Srivastava, C. Norman, F. Azough, M. C. Schäfer, E. Guilmeau, R. Freer, Improving the thermoelectric properties of  $\text{SrTiO}_3$ -based ceramics with metallic inclusions, *Journal of Alloys and Compounds*. 731 (2018) 723–730. doi:10.1016/j.jallcom.2017.10.033.
- [39] J. Y. Cho, O. J. Kwon, Y. K. Chung, J. S. Kim, W. S. Kim, K. J. Song, C. Park, Effect of Trivalent Bi Doping on the Seebeck Coefficient and Electrical Resistivity of  $\text{Ca}_3\text{Co}_4\text{O}_9$ , *Journal of Electronic Materials*. 44 (2015) 3621–3626. doi:10.1007/s11664-015-3924-0.

- [40] T. Mori, T. Hara, Hybrid effect to possibly overcome the trade-off between Seebeck coefficient and electrical conductivity, *Scripta Materialia*. 111 (2016) 44–48. doi:10.1016/j.scriptamat.2015.09.010.
- [41] A. Prytuliak, S. Maruyama, T. Mori, Anomalous effect of vanadium boride seeding on thermoelectric properties of  $\text{YB}_{22}\text{C}_2\text{N}$ , *Materials Research Bulletin*. 48 (2013) 1972–1977. doi:10.1016/j.materresbull.2013.01.043.
- [42] Y. Imai, A. Watanabe, M. Mukaida, Electronic structures of semiconducting alkaline-earth metal silicides, *Journal of Alloys and Compounds*. 358 (2003) 257–263. doi:10.1016/S0925-8388(03)00037-9.
- [43] Y. Katsura, H. Takagi,  $\text{MgSrSi}$ -Type Compounds as a Possible New Family of Thermoelectric Materials, *Journal of Electronic Materials*. 42 (2013) 1365–1368. doi:10.1007/s11664-012-2226-z.
- [44] P. Manfrinetti, M. L. Fornasini, A. Palenzona, The phase diagram of the Ca–Si system, *Intermetallics*. 8 (2000) 223–228. doi:10.1016/S0966-9795(99)00112-0.
- [45] A. Palenzona, M. Pani, The phase diagram of the Sr–Si system, *Journal of Alloys and Compounds*. 373 (2004) 214–219. doi:10.1016/j.jallcom.2003.11.003.
- [46] S. Brutti, D. Nguyen-Manh, D. G. Pettifor, P. Manfrinetti, M. Napoletano, F. Canepa, Electronic, electrical and thermodynamic properties of  $\text{Ca}_5\text{Si}_3$  by first principles calculations and low temperature experimental techniques, *Calphad*. 33 (2009) 260–264. doi:10.1016/j.calphad.2008.07.007.
- [47] T. Inaba, A. Kato, K. Miura, M. Akasaka, T. Iida, Y. Momose, H. Tatsuoka, Preparation and electrical properties of  $\text{Ca}_5\text{Si}_3$  and  $\text{Sr}_5\text{Si}_3$  powders, *Thin Solid Films*. 515 (2007) 8226–8229. doi:10.1016/j.tsf.2007.02.048.
- [48] T. Takeuchi, Conditions of Electronic Structure to Obtain Large Dimensionless Figure of Merit for Developing Practical Thermoelectric Materials, *Mater. Trans.* 50 (2009) 2359–2365. doi:10.2320/matertrans.M2009143.
- [49] C. Wen, T. Nonomura, A. Kato, Y. Kenichi, H. Udono, K. Isobe, M. Otake, Y. Kubota, T. Nakamura, Y. Hayakawa, H. Tatsuoka, Electrical properties of  $\text{Ca}_2\text{Si}$  sintered compact synthesized by spark plasma sintering, *Physics Procedia*. 11 (2011) 106–109. doi:10.1016/j.phpro.2011.01.038.
- [50] C. Wen, T. Nonomura, K. Isobe, Y. Kubota, T. Nakamura, Y. Hayakawa, A. Kato, H. Tatsuoka, Effect of Na Addition on Electric Properties of  $\text{Ca}_2\text{Si}$  Sintered Compacts, *IOP Conf. Ser.: Mater. Sci. Eng.* 18 (2011) 142014. doi:10.1088/1757-899X/18/14/142014.
- [51] G. Balducci, S. Brutti, A. Ciccio, G. Gigli, G. Trionfetti, A. Palenzona, M. Pani, Vapor pressures and thermodynamic properties of strontium silicides, *Intermetallics*. 14 (2006) 578–583. doi:10.1016/j.intermet.2005.10.008.
- [52] J. de Boer, T. Dasgupta, H. Kolb, C. Compere, K. Kelm, E. Mueller, Microstructural effects on thermoelectric efficiency: A case study on magnesium silicide, *Acta Materialia*. 77 (2014) 68–75. doi:10.1016/j.actamat.2014.05.041.



- [53] S. Battiston, S. Fiameni, M. Saleemi, S. Boldrini, A. Famengo, F. Agresti, M. Stingaciu, M.S. Toprak, M. Fabrizio, S. Barison, Synthesis and Characterization of Al-Doped  $\text{Mg}_2\text{Si}$  Thermoelectric Materials, *Journal of Electronic Materials*. 42 (2013) 1956–1959. doi:10.1007/s11664-013-2482-6.
- [54] M. Saleemi, M. S. Toprak, S. Fiameni, S. Boldrini, S. Battiston, A. Famengo, M. Stingaciu, M. Johnsson, M. Muhammed, Spark plasma sintering and thermoelectric evaluation of nanocrystalline magnesium silicide ( $\text{Mg}_2\text{Si}$ ), *Journal of Materials Science*. 48 (2013) 1940–1946. doi:10.1007/s10853-012-6959-0.
- [55] P. Gao, J. D. Davis, V. V. Poltavets, T. P. Hogan, The p-type  $\text{Mg}_2\text{Li}_x\text{Si}_{10.4}\text{Sn}_{0.6}$  thermoelectric materials synthesized by a  $\text{B}_2\text{O}_3$  encapsulation method using  $\text{Li}_2\text{CO}_3$  as the doping agent, *Journal of Materials Chemistry C*. 4 (2016) 929–934. doi:10.1039/C5TC03692E.
- [56] W. G. Zeier, A. Zevalkink, Z. M. Gibbs, G. Hautier, M. G. Kanatzidis, G. J. Snyder, Thinking Like a Chemist: Intuition in Thermoelectric Materials, *Angew. Chem. Int. Ed*. 55 (2016) 6826–6841. doi:10.1002/anie.201508381.
- [57] W. Xie, X. Tang, Y. Yan, Q. Zhang, T. M. Tritt, Unique nanostructures and enhanced thermoelectric performance of melt-spun  $\text{BiSbTe}$  alloys, *Appl. Phys. Lett.* 94 (2009) 102111. doi:10.1063/1.3097026.
- [58] C. S. Lue, C. N. Kuo, J. Y. Huang, H. L. Hsieh, H. Y. Liao, B. Ramachandran, Y. K. Kuo, Enhancement of thermoelectric performance driven by Ge substitution in  $\text{SrSi}_2$  alloy, *Journal of Physics D: Applied Physics*. 46 (2013) 315303. doi:10.1088/0022-3727/46/31/315303.
- [59] J. Mackey, F. Dynys, A. Sehirlioglu, Si/Ge– $\text{WSi}_2$  composites: Processing and thermoelectric properties, *Acta Materialia*. 98 (2015) 263–274. doi:10.1016/j.actamat.2015.07.025.
- [60] P. Nieroda, J. Leszczynski, A. Kolezynski, Bismuth doped  $\text{Mg}_2\text{Si}$  with improved homogeneity: Synthesis, characterization and optimization of thermoelectric properties, *Journal of Physics and Chemistry of Solids*. 103 (2017) 147–159. doi:10.1016/j.jpcs.2016.11.027.
- [61] D. G. Cahill, S. K. Watson, R. O. Pohl, Lower limit to the thermal conductivity of disordered crystals, *Phys. Rev. B*. 46 (1992) 6131–6140. doi:10.1103/PhysRevB.46.6131.
- [62] M. Ioannou, G. S. Polymeris, E. Hatzikraniotis, K. M. Paraskevopoulos, T. Kyratsi, Effect of Bi-doping and Mg-excess on the thermoelectric properties of  $\text{Mg}_2\text{Si}$  materials, *Journal of Physics and Chemistry of Solids*. 75 (2014) 984–991. doi:10.1016/j.jpcs.2014.04.008.

